Results in Engineering 26 (2025) 105657

Contents lists available at ScienceDirect

Results in Engineering

journal homepage: www.sciencedirect.com/journal/results-in-engineering

Research paper

Experimental and numerical study of seismic performance and failure mechanisms of multi-story elliptic and Quasi-X braced resisting frames

Younes Nouri [a], Habib Ghasemi Jouneghani [b], Abbas Haghollahi [b], Parham Memarzadeh [c,d,*], Ehsan Hemati [b]

[a] Department of Civil Engineering, Ferdowsi University of Mashhad, Mashhad, Iran
[b] Department of Civil Engineering, Shahid Rajaee Teacher Training University, Tehran, Iran
[c] Department of Civil Engineering, Na.C., Islamic Azad University, Najafabad, Iran
[d] Sustainable Development in Civil Engineering Research Center, Na.C., Islamic Azad University, Najafabad, Iran

ARTICLE INFO

Keywords:
Elliptic braced resisting frames
Quasi-X braced resisting frames
Failure mechanisms
Seismic performance factors
Experimental study
Finite element analysis

ABSTRACT

Over the past few years, the development of Elliptic and Quasi-X bracing systems has introduced innovative approaches to structural reinforcement. While Elliptic Braced Resisting Frames (ELBRFs) have been extensively studied in both single-story and multi-story configurations, empirical data on Quasi-X Braced Resisting Frames (QXBRFs) remain limited. This gap has raised concerns about the reliability of numerical simulations for QXBRFs. To address this, the present study experimentally investigates the seismic behavior and failure mechanisms of multi-story QXBRFs, comparing their performance with ELBRFs. By providing experimental data for multi-story QXBRFs, this study contributes to the validation of numerical models and a deeper understanding of their seismic properties. Laboratory tests are conducted using 1/6-scale, single-span, four-story models of both ELBRF and QXBRF under cyclic quasi-static loading. Various seismic performance indicators—including stiffness, ductility, strength, failure modes, and energy dissipation—are assessed. In addition, nonlinear finite element method (FEM) analyses benchmark the seismic performance of QXBRFs against ELBRFs and traditional X-braced frames under similar loading conditions. The results confirm the seismic behaviors and failure patterns observed in the experimental tests. Findings indicate that incorporating elliptic and Quasi-X braces into moment frame systems significantly enhances seismic performance. The yielding of these braces delays column failure, allowing the structure to withstand substantial nonlinear deformations before collapse. In both systems, yielding initiates in the lower stories and progresses upward, eventually affecting the columns. However, QXBRFs exhibit more pronounced strength degradation at higher displacements compared to ELBRFs. These results highlight the effectiveness of these bracing systems in improving structural resilience and safety during earthquakes. Moreover, the response modification factors for ELBRFs and QXBRFs are calculated as 7.3 and 6.8, respectively. The theoretical predictions from numerical models closely align with experimental findings, reinforcing confidence in the design and application of these bracing systems for seismic resistance.

1. Introduction

In most structural design codes, a key aspect of seismic design for various lateral load-resisting systems is the determination of appropriate Seismic Performance Factors (SPFs) [1]. Simply put, seismic design must satisfy two essential criteria: adequate stiffness and sufficient resistance. In addition, structures must possess enough ductility to effectively dissipate energy during major seismic events [2–5]. Meeting these objectives depends on the careful selection of SPFs during the seismic design process. Over the past two decades, numerous studies have explored the seismic performance of single-story and multi-story lateral bracing systems under cyclic quasi-static loading. For instance, Tong et al. [6] investigated the cyclic behavior of two-story, single-span steel frame structures with composite reinforced concrete infill walls and partially restrained connections at a one-third scale. Their findings indicated that this system could serve as an effective lateral resistance mechanism for low- to moderate-rise buildings in seismic regions, providing both adequate strengths to withstand lateral forces and

---

[*] Corresponding author at: Department of Civil Engineering, Na.C., Islamic Azad University, Najafabad, Iran.
E-mail address: parham.memarzadeh@iau.ac.ir (P. Memarzadeh).

https://doi.org/10.1016/j.rineng.2025.105657
Received 7 April 2025; Received in revised form 23 May 2025; Accepted 6 June 2025

sufficient stiffness to limit drift. Zhou et al. [7] examined the seismic performance of an eight-story steel staggered-truss system using a 1/8-scale model under reversed cyclic loading through both experimental and finite element (FE) modeling. They evaluated key seismic performance indices such as yield load, ductility, strength, deformation, energy dissipation, and rigidity degradation. The findings of Zhou et al. showed that increasing the structural height initially enhances the ductility factor but subsequently leads to a decline. Additionally, as the height-to-width ratio of the structure increases, the top displacement rises, while ductility decreases. In another investigation, Liu et al. [8] analyzed the hysteretic behavior and failure mechanisms of a full-scale, two-story, corner-supported modular steel structure with vertical inter-module connections under cyclic loading. Results showed that ductile failure occurred, characterized by buckling at the ends of the ceiling and floor beams as well as at the lower column bases.

The proper selection of seismic performance factors (SPFs) remains a critical aspect of structural design, significantly influencing the evaluation of seismic behavior. Over the past decades, extensive research has provided valuable insights into the failure mechanisms and seismic performance of various structural systems, forming the foundation for assessing and improving existing models [9–18].

In the past two decades, the interaction between structure and architecture has led to the introduction of innovative seismic-resistant structural systems. These systems aim not only to create proper stiffness and ductility in structures from a structural perspective but also to provide sufficient space for openings without creating limitations in the architecture. A prime example of this innovation is the ELBRF, developed by Ghasemi Jouneghani et al. [19]. The ELBRF successfully fulfills seismic performance criteria while simultaneously providing greater architectural flexibility [20–22]. The seismic behavior of single-story ELBRFs has been comprehensively investigated through both experimental and numerical studies [23–25]. In another study, Ghasemi Jouneghani and Haghollahi [26] investigated the seismic behavior of 3-, 5-, and 7-story steel moment frames equipped with elliptic braces through Incremental Dynamic Analysis (IDA). The results indicated a response modification factor of 6.5 (ultimate limit state method) and 9.5 (allowable stress method). Further investigations have compared the seismic behavior and failure modes of ELBRFs with various other bracing systems like X-bracing, K-bracing, knee bracing, and diamond bracing, focusing on single-frame setups [27]. Ghasemi Jouneghani et al. [28,29] were the first to introduce accurate theoretical equations for calculating the elastic stiffness of two-dimensional, single-story single-span, as well as multi-story multi-span steel frames, including those equipped with elliptic braces. These equations were found to have very slight variations from the elastic stiffness values calculated via FEMs. In 2024, a study [30] evaluated the seismic performance factors of frames equipped with elliptic braces and rotational friction dampers using incremental dynamic analysis. Subsequently, Ghasemi Jouneghani et al. [31] explored the seismic performance and failure mechanisms of 1/6 scale single-span, four-story ELBRFs and two-span, four-story Mega Elliptic Braced Resisting Frames (MELBRFs). The seismic behavior of the proposed specimens was then compared with other types of bracing systems such as X-, V-, Inverted-V, Two-Story X-, and Two-tiered diagonal braced frames in a story-base model under cyclic quasi-static loading through nonlinear FEM analyses. The findings indicated that the yielding of elliptic braces would delay the failure mode of adjacent elliptic columns, thus helping tolerate significant nonlinear deformation to the point of ultimate failure.

In other investigations, Shirpour and Fanaie [32–35] conducted a comprehensive assessment of the seismic performance indicators for steel moment frames equipped with various bracing setups, including quarter-elliptic braced (QEB-MFs), half-elliptic braced (HEB-MFs), and Quasi-X braced (QXB-MFs), utilizing the rigorous FEMA P695 methodology.

In recent decades, researchers have evaluated the seismic performance of the innovative Elliptic-Braced Resisting Frames (ELBRFs) only in single-story single-span configurations. Although numerical studies have investigated the behavior of multi-story ELBRF configurations, the lack of laboratory data has cast doubt on the reliability of these numerical results. To address this gap in knowledge, this article evaluates the seismic performance and failure mechanisms of multi-story ELBRFs through a laboratory program and compares them with a developed type of this bracing system known as Quasi-X Braced Resisting Frames (QXBRFs). The key contribution of this research is the provision of laboratory test data for multi-story ELBRF and QXBRF systems, which can be utilized to validate numerical models and investigate their seismic characteristics. This study begins with an overview of the ELBRF and QXBRF systems before evaluating the seismic behavior and energy dissipation capacity of a 1/6-scale, single-span, four-story QXBRF specimen subjected to cyclic quasi-static loading through experimental testing, with results compared to those of an ELBRF specimen. It also computes Seismic Performance Factors (SPFs), including the overstrength factor (Ω), ductility factor (R_μ), and response modification factor (R), for multi-story ELBRF and QXBRF systems. Additionally, failure mechanisms are investigated through experimental programs, while numerical validation of failure mechanisms and seismic performance is conducted using nonlinear FEM analysis. Finally, the actual behavior of the QXBRF specimen is compared to that of elliptic braced and X-braced frames in a base story using nonlinear FEM analyses.

2. Seismic behavior of steel braced structures

2.1. Conventional braced frames

Diagonal-braced frames (DBFs) consist of a single diagonal member per span (Fig. 1a). Despite their simplicity, DBFs are prone to soft-story mechanisms, overall instability under large deformations, and unsustainable and asymmetric cyclic behavior. Inverted V-braced frames (IVBFs), while providing high initial stiffness and strength, suffer from weak post-buckling behavior (Fig. 1b). Buckling of compressive members in a specific story generates unbalanced vertical forces at beam midspans, leading to localized damage and potential collapse. Typical CBFs, such as X-braced (cross-braced) frames, are widely employed to resist lateral loads but are susceptible to compression-induced buckling (Fig. 1c). This instability occurs before reaching yield strength and results in asymmetric behavior under tension and compression, undermining energy dissipation and causing significant damage to both structural and non-structural components. On the other hand, the application of MRFs, as one of the most commonly used lateral load-resisting systems for steel structures, is limited due to high stress concentration at beam-to-column connections, low lateral stiffness, extensive damage under strong earthquakes, and economic constraints (Fig. 1d).

2.2. Curve braced frames

Positioned in the middle bay of a building's facade, curve braces help maintain the aesthetic openness of the facade while enhancing the structure's performance. These braces come in various forms, including quarter-elliptic, half-elliptic, Quasi-X, and elliptic shapes. Among the latest lateral load-resisting systems is the quarter-elliptic braced resisting frame (QEBRF), shown in Fig. 2a. This system combines a moment-resistant frame with a quarter-elliptic brace. Unlike diagonal braces, the quarter-elliptic bracing system exhibits symmetrical behavior in both tension and compression, ensuring consistent energy dissipation during seismic events. Another innovative lateral load-resisting system is the Half-Elliptic Braced Resisting Frame (HEBRF), depicted in Fig. 2b. This configuration uses two quarter-elliptic braces to address the shortcomings of traditional inverted V-braced frames (IVBFs). The half-elliptic shape helps balance forces and reduce deflections at the mid-span of beams, while improving energy absorption. HEBRFs reduce the risk of soft first stories and structural instability by demonstrating hardening

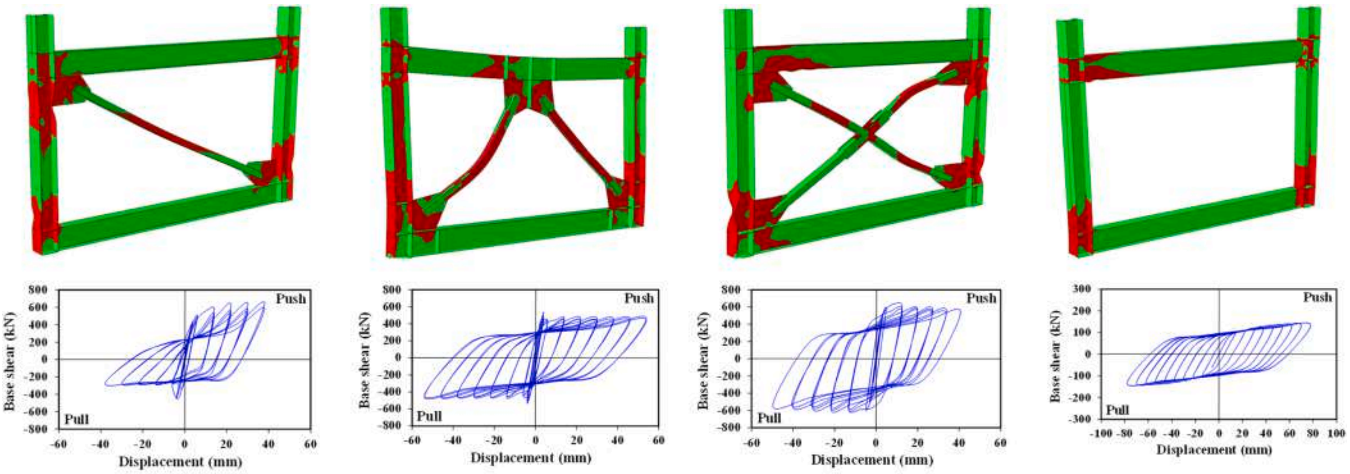

(a) Diagonal-braced frames (DBFs)

(b) Inverted V-braced frames (IVBFs)

(c) X-braced moment frames (XB-MFs)

(d) Moment resisting frames (MRFs)

Fig. 1. Schematic diagram for seismic behavior evaluation of conventional braced frames.

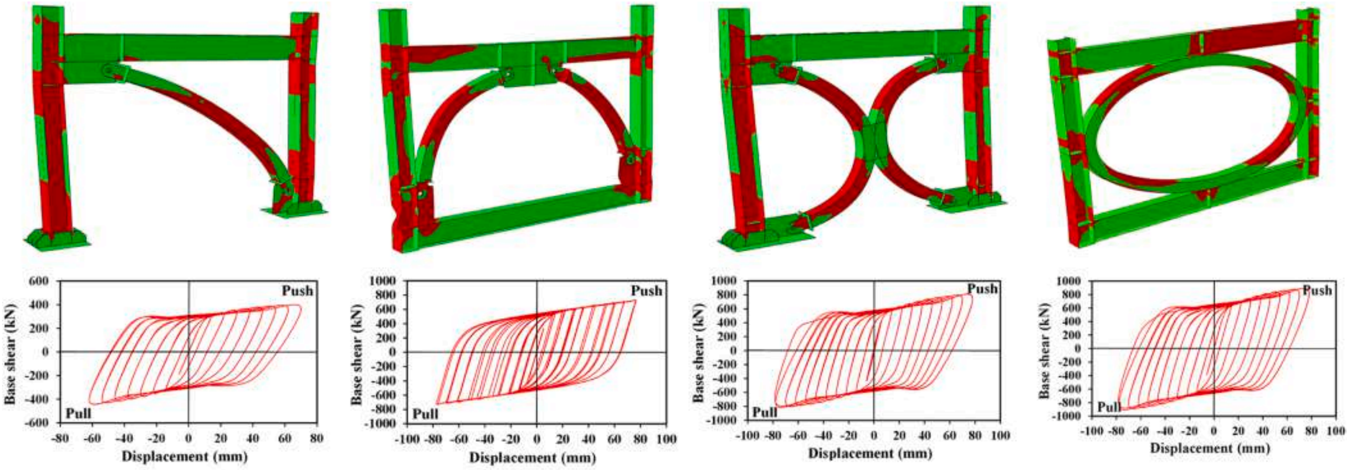

(a) Quarter-elliptic braced resisting frames (QEBRFs)

(b) Half-elliptic braced resisting frames (HEBRFs)

(c) Quasi-X braced resisting frames (QXBRFs)

(d) Elliptic braced resisting frames (ELBRFs)

Fig. 2. Schematic diagram for seismic behavior evaluation of curve braced frames.

behavior under large deformations and symmetrical cyclic performance. In contrast, the Quasi-X Braced Resisting Frames (QXBRFs), shown in Fig. 2c, use four quarter-elliptic braces to enhance ductility and energy dissipation. This design reduces the likelihood of a soft-story occurrence and helps maintain stability under significant deformations. The Quasi-X bracing serves as an effective alternative to Buckling-Restrained Braces (BRBs), offering consistent cyclic behavior and energy dissipation without sacrificing stiffness or strength. A distinctive feature of this system is that the bracing members do not directly connect to the frame's columns and beams, providing an advantage over both circular and elliptic bracing systems. Elliptic Braced Resisting Frames (ELBRF), illustrated in Fig. 2d, use four quarter-elliptic braces attached at specific lengths to the frame's columns and beams. This system maximizes space for openings. The force transmission path of the elliptic braces, which are positioned at the center of the columns, does not align perpendicular to the vertical axis, thus preventing column buckling. This gives the system distinct behavior compared to K-braces and diamond braces. The elliptic bracing system demonstrates symmetric behavior under both compression and tension in its hysteresis curve, maintaining strength and stiffness without degradation.

3. Experimental program

An experimental test program was developed to assess the performance of two types of multi-story structural systems: ELBRF and QXBRF. The test specimens were subjected to cyclic loading to evaluate their structural behavior and response. This study marks the first time the seismic performance and failure mechanisms of a multi-story QXBRF are evaluated through an experimental program, with the results compared to those of the ELBRF specimen. Additionally, comparisons were made with traditional X-braced frames using nonlinear Finite Element Method (FEM) analyses, specifically focusing on the base story level.

3.1. *Description of test specimen*

To evaluate the seismic performance, hysteretic behavior, and failure mechanisms of the ELBRF and QXBRF systems, two-dimensional, single-span, four-story frames were designed and constructed. One frame was for the ELBRF, and the other for the QXBRF. Both test specimens were scaled down with a ratio of 1:6. Fig. 3 provides detailed specifications of the ELBRF and QXBRF test specimens. The columns and beams of the frames were made from steel boxes with dimensions of 40×20×2 *mm*, while the braces were constructed from steel boxes measuring 20×20×0.9 *mm*. The total height of each frame is 2115 *mm*, with each story height set at 520 *mm* and a beam length of 1000 *mm*. Figs. 3 and 4 illustrate the placement of strain gauges and Linear Variable Differential Transformers (LVDTs) for both systems.

The base plates, measuring 250×250×10 *mm*, were welded directly to the columns. To improve connection rigidity and prevent deformation, three 80×40×3 *mm* triangular stiffeners were welded between the columns and base plates. Each base plate was secured to the lab's reaction frame using four M30 high-strength bolts. Additionally, to control out-of-plane movements, two lateral restraint systems made of 40×40×3 *mm* angle profiles were fixed to the sides of the frame. Table 1 provides further details on the sections used in the construction of both the ELBRF and QXBRF specimens.

The initial test specimen, referred to as the ELBRF, was established as a reference system for lateral force resistance by integrating a steel moment frame with an elliptic brace system. These elliptic braces contribute significantly to both the lateral stiffness and energy dissipation capabilities of each floor. To ensure accurate shaping of the elliptic brace while minimizing residual stresses, four quarter-elliptic braces were used per story, with each brace joined at both ends (see Fig. 3). Each elliptic brace is connected to the beams and columns via a 4 *mm* thick auxiliary plate, which is fully welded to the beams, columns, and braces. This connection method helps reduce stress concentrations by increasing the contact area.

The second specimen, QXBRF, is similar to the ELBRF in that it uses four quarter-elliptic braces in each span of the frame. However, in the QXBRF, the ends of the quarter-elliptic braces are connected to gusset plates located at the corners of the frame, while the other ends are joined together using two auxiliary plates at the center of the frame (see Fig. 4). Similar to the ELBRF, a beam is used to connect the elliptic braces at the lower axis of this specimen. Unlike the ELBRF, however, the bracing members in the QXBRF do not connect directly to the frame members (columns and beams), offering an advantage over circular and elliptic bracing systems (Fig. 4).

To accurately shape the quarter-elliptic braces and minimize residual stresses, a hydraulic three-roller bending roll was utilized for each brace. For proper connectivity between the quarter-elliptic braces in both the ELBRF and QXBRF specimens, Tungsten Inert Gas (TIG) welding was employed, considering the 2 *mm* thickness of the beam and column cross-sections. The beam-to-column connection is designed as direct moment connections with full penetration welds (Fig. 5).

3.2. *Scaling process of the specimens*

Due to the limitations of the structural laboratory facilities, it was not feasible to construct the braced frames at their real dimensions. Therefore, the authors adopted a scaled-down approach while preserving the geometric proportions of the sections (including the moment of inertia and cross-sectional area). Since I-shaped sections were impractical at the reduced scale, equivalent box-shaped sections were used to maintain the closest possible resemblance to the real structure. Specific implementation details, such as the use of stiffeners at beam-column connections (Fig. 6), were incorporated to simulate clamped supports accurately. The primary scaling criterion was geometric similarity, and to minimize distortions, the structural responses under applied loads were carefully matched to those expected in the full-scale structure, ensuring the reliability of the scaled-down model [36–38].

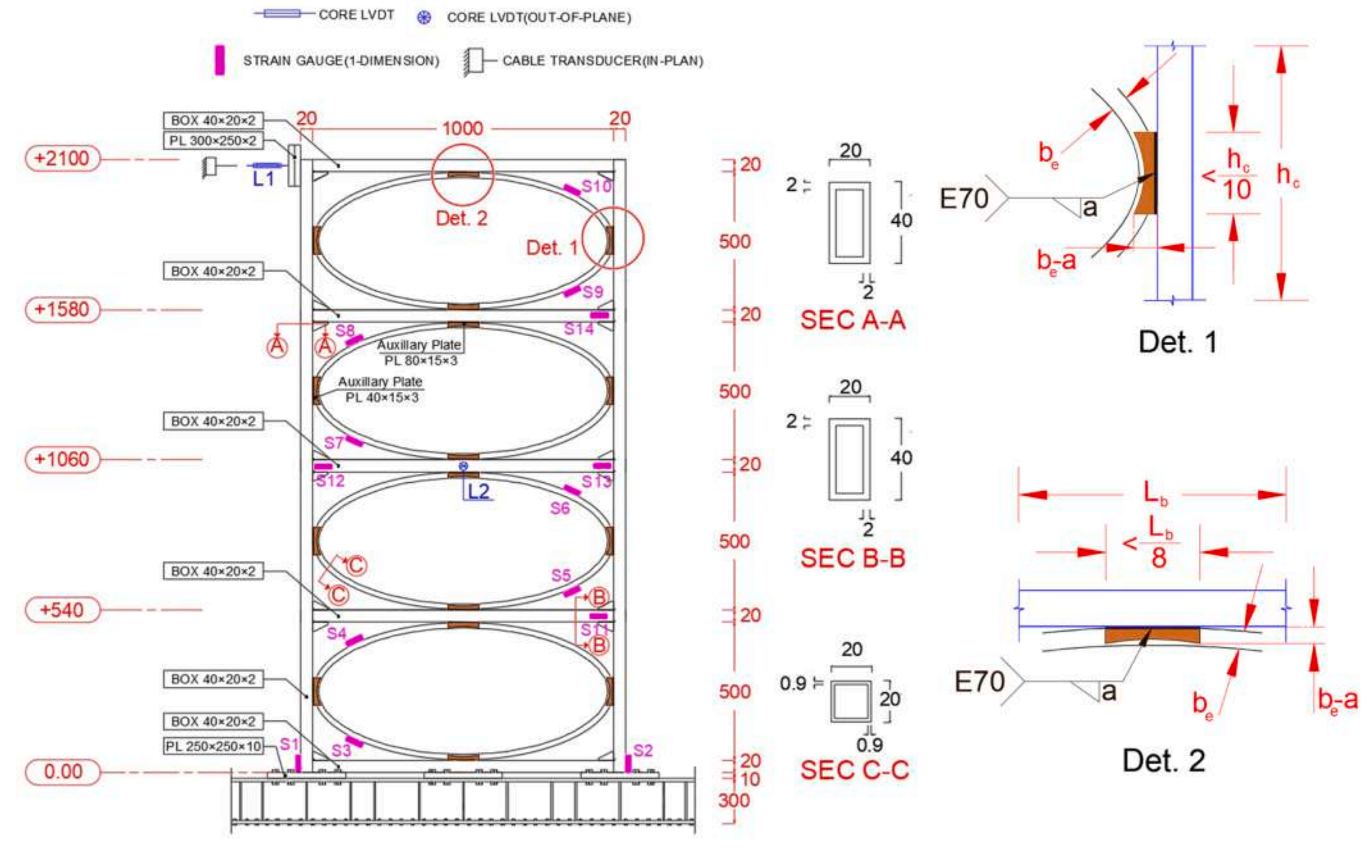

Fig. 3. Dimensions, sections, and measuring instruments in ELBRF [31].

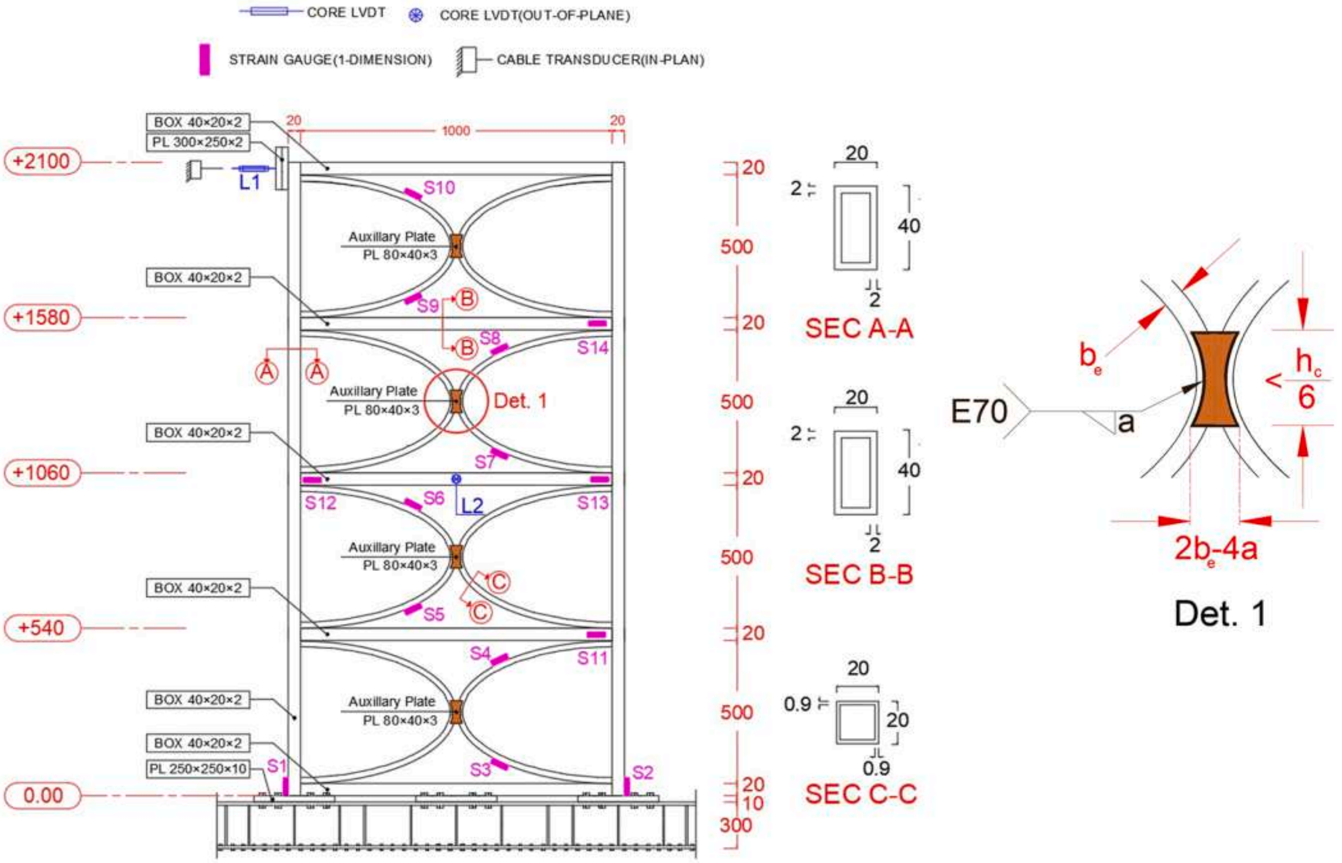

Fig. 4. Dimensions, sections, and measuring instruments in QXBRF.

Table 1
. Cross sectional and dimension of specimens.

Specimen	Beam (*mm*)	Column (*mm*)	Quarter-elliptic brace (*mm*)	Elliptic brace (*mm*)
ELBRF	BOX 40×20×2*	BOX 40×20×2*	BOX 20×20×0.9**	BOX 20×20×0.9**
QXBRF	BOX 40×20×2*	BOX 40×20×2*	BOX 20×20×0.9**	BOX 20×20×0.9**

* Nominal thickness is 2.0 *mm* and the measured thickness is 2.20 *mm*.
** Nominal thickness is 0.9 *mm* and the measured thickness is 1.0 *mm*.

The original prototype structure was designed based on a typical mid-rise building, and the scale factor was applied to the experimental models, considering the following scaling laws. This study adopted a 1/6 geometric scale factor due to laboratory constraints, with all linear dimensions scaled uniformly while maintaining stiffness equivalence through proportional section properties (area $\sim(1/6)^2$, moment of inertia $\sim(1/6)^4$). The prototype steel material (Grade ST37) was used without scaling to preserve authentic stress-strain behavior, consistent with standard practice for elastic-plastic analyses. Static loads were scaled by $(1/6)^2$ to ensure stress equivalence.

The quasi-static loading rate (0.2 *mm/s*) was selected to minimize strain-rate effects. The adopted cyclic protocol (ATC-24) effectively captures cumulative damage characteristics while enabling direct comparison with existing studies. Although this approach provides reliable energy dissipation metrics under quasi-static conditions, dynamic loading rates may influence hysteretic behavior and should be investigated separately.

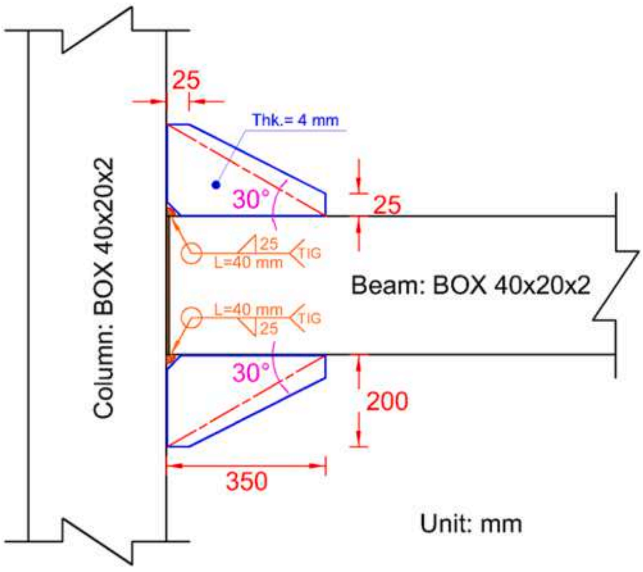

Fig. 5. The details of beam-to-column connection equipped with two stiffeners.

3.3. Material properties

The mechanical characteristics of the steel materials used for the beams, columns, and braces in both the ELBRF and QXBRF models were determined through standard tension coupon tests, following the ASTM A370 guidelines [36]. The properties measured include elastic modulus (E_s), yield tensile strength (f_y), thickness (t_s), ultimate tensile strength

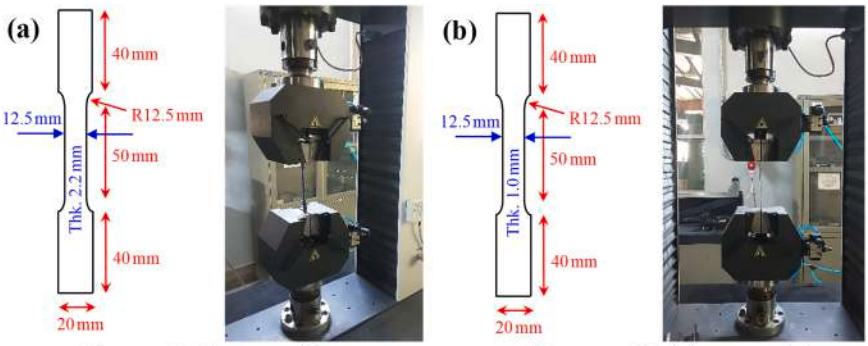

(a) beam and column material

(b) quarter-elliptic brace material

Fig. 6. Dimension of coupon test for different thickness.

(f_u), and elongation (ξ). These samples were extracted from the plates used in constructing the specimens, as shown in Fig. 6. The results of these tests, detailing the specimens' mechanical properties, are summarized in Table 2. As specified in AISC 360-16 [37], material property tests were conducted on three coupons for each structural component (beams, columns, and elliptical braces) to ensure statistical reliability. The average values of these tests were reported in the manuscript, Table 2.

3.4. *Test setup and instrumentation*

The experimental tests for the ELBRF and QXBRF specimens were carried out in the structural laboratory at the Islamic Azad University of Najafabad. Figs. 7 and 8 illustrate the experimental setup for both types of specimens. The specimens were anchored to the laboratory's reaction frame, which is equipped with a strong floor for enhanced stability. Both frames were positioned between two columns of the reaction frame and secured to the strong base using fixed supports. To prevent out-of-plane movement and ensure the frames' stability, two Λ-frames were installed on either side at the third-story level, as shown in Figs. 7 and 8. This technique, which has been previously utilized, effectively controls unwanted deflections during testing [23]. Cyclic loading was applied using a hydraulic jack placed at the center of the beam at the highest level, ensuring no secondary moments from jack eccentricity. The actuator was attached to one of the columns of the reaction frame. A steel plate, measuring 350×250×20 *mm*, was welded onto each specimen and connected to the actuator using eight high-strength M24 bolts (see Figs. 7 and 8).

The actuator was capable of applying a maximum push-pull force of ±600 kN and achieving a maximum displacement of ±200 *mm*, with a loading rate set at 10 *mm/min*. For displacement measurements, two Linear Variable Differential Transformers (LVDTs) were used. One LVDT was positioned at the second story to measure out-of-plane displacement, while the in-plane displacement was recorded by the actuator's built-in deformation measurement system. Fourteen strain gauges (S1–S14) were strategically placed at expected plastic hinge locations on the beams, columns, and quarter-elliptic braces, determined through numerical simulation using Abaqus software [38]. Figs. 7 and 8 illustrate the overall test configuration, including the actuator's placement, support conditions of the frame, positioning of LVDTs (L1 and L2), and locations of strain gauges (S1–S14).

Table 2
Mechanical properties of sections.

Section	Gauge Length (mm)	Yield Strength (MPa)	Module of Elasticity (GPa)	Elongation (%)
Beam	50	289	202.1	37
Column	50	289	202.1	37
Quarter-elliptic brace	50	293	201.3	34

3.5. *Strain measurement*

In this research, strain gauges were employed to measure axial strain at various points across the specimens, which is essential for evaluating structural integrity and performance in both research and practical applications [39]. These gauges were strategically placed on different surfaces of the steel frameworks, with their exact positions determined through finite element modeling of the specimens. The placement of the strain gauges is illustrated in Figs. 3 and 4.

3.6. *Loading history*

One critical element in assessing the seismic behavior of structures involves selecting an appropriate loading pattern. In this study, lateral quasi-static loading was applied to evaluate the seismic performance of both ELBRF and QXBRF specimens. This process involved defining parameters such as the number of loading cycles, load range, frequency, and the type of loading at each stage.

The lateral loading history for the cyclic testing of these multi-story structures (see Fig. 9) followed the ATC-24 [40] protocol. The amplitude of cyclic loading was increased up to seven times the yielding deformation (δ_y). The yield displacement (δ_y) was determined through finite element analysis using Abaqus software [38], considering the change in stiffness between the elastic and post-yield phases. The load was applied at the beam-to-column connection within the plane of the frame.

The cyclic loading sequence consisted of two distinct phases: the elastic phase and the plastic phase. During the elastic phase, the specimens underwent three cycles at drift ratios of 0.33% and 0.67%. In the subsequent plastic phase, the drift ratio was progressively increased from 1.0% to 7.0%, continuing until structural failure. The target displacement was set at 140 *mm*, corresponding to a 7.0% drift ratio. Both ELBRF and QXBRF specimens were tested in accordance with the ATC-24 protocol, as shown in Fig. 9.

4. Experimental results

4.1. *Test observations*

The experimental observations during the cyclic quasi-static loading tests of the specimens are discussed separately below.

4.1.1. *ELBRF Specimen*

The ELBRF specimen was the first to undergo cyclic quasi-static loading tests, serving as a baseline for evaluating and comparing seismic performance with the QXBRF specimen. To identify yielding

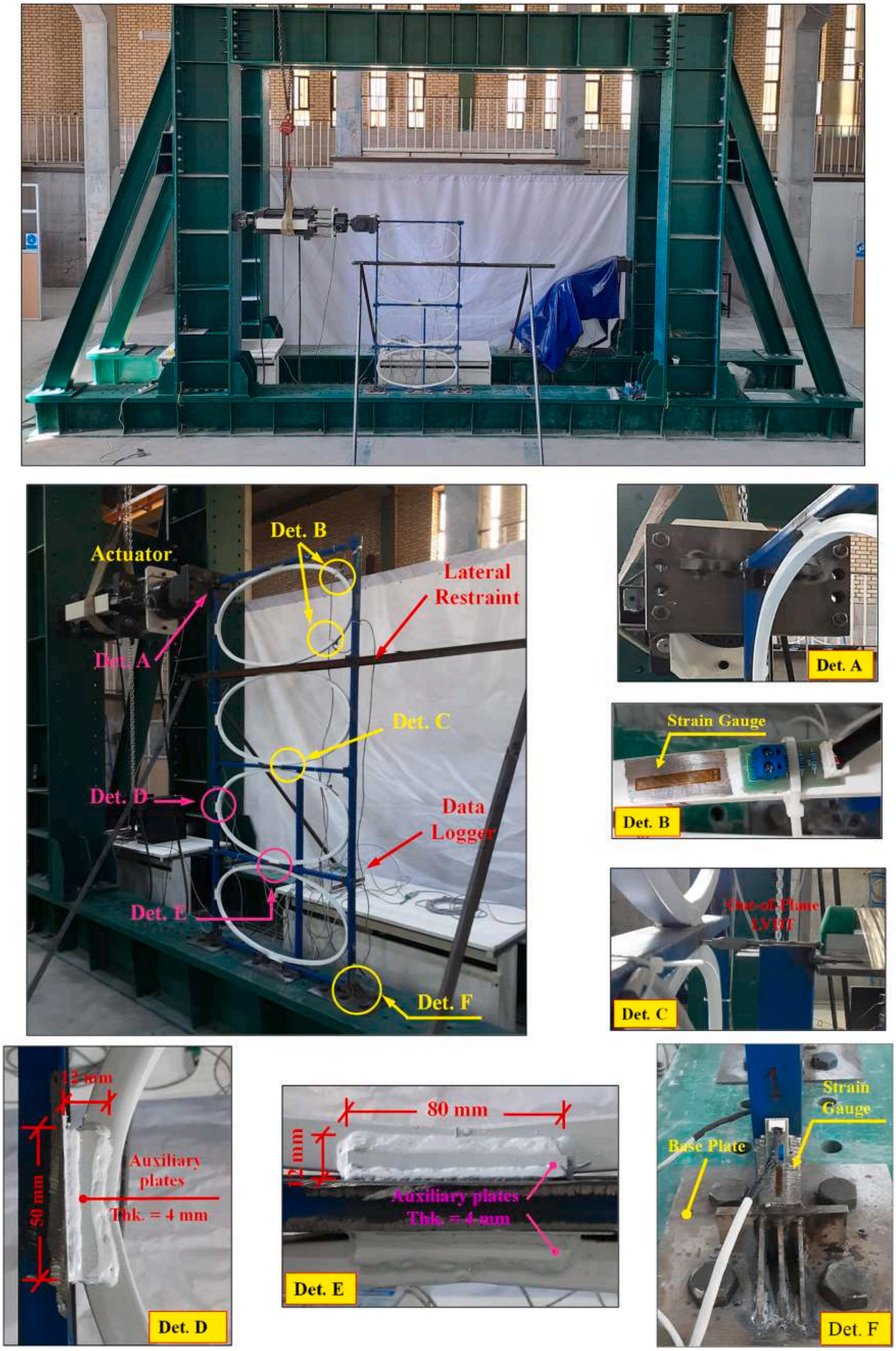

Fig. 7. Test set-up configuration, Strain gauges, and out-of-plane LVDT in ELBRF specimen.

Fig. 8. Test set-up configuration, Strain gauges, and out-of-plane LVDT in QXBRF specimen.

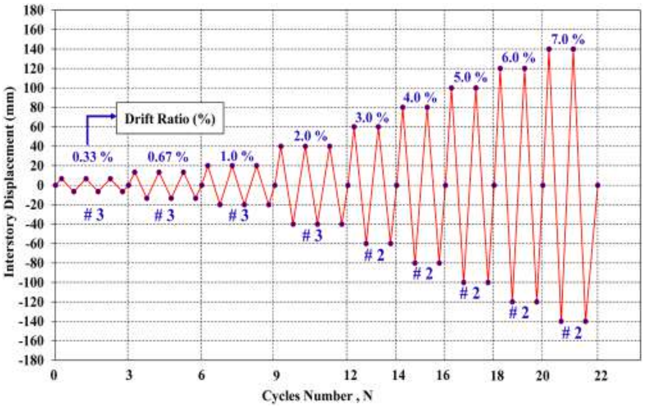

Fig. 9. Cyclic protocol based on ATC-24 [40].

locations, the surfaces of the beams, columns, and elliptic braces were coated with a quick-drying paint that peels upon plastic deformation. Fig. 10 illustrates various deformation stages of the elliptic braced frame under lateral loading. At the beginning of the test (Fig. 10a), the specimen was well-aligned in both the in-plane and out-of-plane directions. In accordance with the cyclic loading protocol shown in Fig. 9, the load was gradually increased until yielding, deformation, or buckling was observed in the structural elements. Testing continued with progressively larger displacement increments until the specimen reached failure. At low displacement levels (0.33% to 0.67% δy), deformations were negligible. Once the drift reached the yield displacement (δ_y), as shown in Fig. 10b, minor plastic deformations emerged in the elliptic braces, indicated by slight discoloration. Further details on yielding behavior are discussed later in the strain gauge analysis. At a displacement of 20 *mm* (equivalent to a 1.0% drift), the ELBRF specimen exhibited largely linear behavior (Fig. 10b). The frame successfully withstood significant plastic deformation during 22 loading cycles, reaching drift levels of 4.0% to 7.0% (Fig. 10c–h). Initial brace deformations were observed at a 40 *mm* displacement ($\theta = 2.0\%$), where the elliptic braces began to deform in-plane (Fig. 10c). The ELBRF specimen demonstrated increased lateral resistance at displacements of 60 *mm* and 80 *mm* ($\theta = 3.0\%$ and $\theta = 4.0\%$, respectively). At these levels, substantial in-plane deformations developed, particularly in the second- and third-story braces (Fig. 10d). When the displacement reached 80 *mm* and 100 *mm* (4.0% and 5.0% drift), all braces experienced noticeable deformation due to alternating tension and compression forces. These braces functioned as ductile fuses, enhancing the system's ductility (Fig. 10e, f). In the final loading cycles, at displacements of 120 *mm* and 140 *mm* (6.0% and 7.0% drift), the ELBRF specimen demonstrated pronounced ductility. No lateral-torsional buckling was observed in the beams, nor did the columns experience out-of-plane buckling. The columns maintained stability even under large displacements (Fig. 10g, h). These observations suggest that the curved geometry of the elliptic braces facilitates rapid transitions from tensile to compressive forces with each reversal of loading direction, thereby limiting permanent deformation and preventing out-of-plane buckling. Once lateral loading ceased and the actuator was removed, the elliptic braces returned to their original shape, as shown in Fig. 10i.

The final state of the frame featured notable deformations, wrinkling in the braces, and plasticity in the beams and columns. Nevertheless, the overall structural integrity of the frame was maintained beyond the yield point, with no significant buckling or fractures at beam-to-column or brace-to-frame welded connections. The welded joints, made through auxiliary plates [23–25,27], did not experience fracture, although minor plastic deformation was observed above these connections during the final stages of loading.

4.1.2. QXBRF specimen

The QXBRF specimen, representing an alternative configuration of curved braced frames, was tested to evaluate its seismic behavior in comparison to the ELBRF. Similar to the ELBRF, the surfaces of the structural elements in the QXBRF were coated with fast-drying paint to facilitate the identification of yield points and areas of plastic deformation. The deformation progression of the QXBRF specimen during the cyclic loading test is documented step by step in Fig. 11.

At the beginning of the test (Fig. 11a), the load was gradually increased. At a displacement of 13.4 mm, corresponding to a 1% drift, no plastic deformations were observed during the cycles at 0.33 δ_y and 0.67 δ_y, and the specimen exhibited elastic behavior. The quarter-elliptic braces within the frame deformed from their original configuration and returned to their initial shape during these cycles. However, at displacements corresponding to δ_y, pale discoloration began to appear on the braces, as shown in Fig. 11b.

As the lateral load increased, by the 10th cycle at a drift angle of $\theta = 2.0\%$, deformations began to emerge in the structural members, particularly in-plane deformation of the quarter-elliptic braces. With further increases in lateral load, plastic deformations developed at the mid-span of the quarter-elliptic braces, as illustrated in Fig. 11c. The lateral resistance of the structure continued to rise until a displacement of 60 *mm* ($\theta = 3.0\%$ drift) was reached, at which point significant deformations were observed in the quarter-elliptic braces across the second to fourth stories (Fig. 11d).

At this stage, some of the quarter-elliptic braces in the upper stories exhibited plastic deformation and wrinkling at displacements corresponding to 3 δy. At 4 δy, cracking occurred in one of the welds at the brace-to-column connection, leading to partial separation; however, the remaining connections remained intact, as illustrated in Fig. 11e.

In-plane deformations persisted up to a displacement of 100 *mm*, corresponding to a 5% drift (Fig. 11f), at which point the quarter-elliptic braces on the second to fourth stories became fully wrinkled and deformed, having reached 5 δy. Cracks also appeared in some previously undamaged connections.

During the final loading cycles, the QXBRF specimen demonstrated high ductility, with no signs of buckling in the beams or columns (Fig. 11g and 11h). A crack was identified in the base plate connection at displacements of 6 δy and 7 δy. Fig. 11h captures the ultimate deformation state of the frame, revealing widespread plastic deformation and wrinkling in the quarter-elliptic braces across all stories.

The seismic response of the QXBRF specimen was comparable to that of the ELBRF. The quarter-elliptic braces rapidly transitioned between tension and compression during cyclic loading, effectively mitigating out-of-plane buckling and limiting permanent deformations. Following the conclusion of lateral loading and disconnection of the actuator, the braces returned to their original configuration, as shown in Fig. 11i.

4.2. Hysteretic behavior of specimens

To assess the cyclic performance, efficiency, strength, stiffness, ductility, overstrength, deterioration in stiffness and strength, equivalent hysteresis damping coefficient, seismic performance factors, and energy absorption capabilities of the ELBRF and QXBRF systems during various stages of cyclic quasi-static loading, experimental hysteresis curves plotting shear strength against displacement are employed. Figs. 12 and 13 illustrate the experimental hysteresis curves of the ELBRF and QXBRF, highlighting the significant loading stages.

In this study, positive load values signify tension, while negative values indicate compression within the members of the specimens. This convention is consistently applied across all load-displacement plots. The hysteresis curves of both the ELBRF and QXBRF specimens demonstrate three well-defined phases:

1. **Elastic Stage:** In this region, the response of the structure is linear, with deformation recovering once the load is removed.

(a) Start loading

(b) at 20 *mm* displacement, equivalent to 1.0% drift, in cycle 9

(c) at 40 *mm* displacement, equivalent to 2.0% drift, in cycle 12

(d) at 60 *mm* displacement, equivalent to 3.0% drift, in cycle 14

(e) at 80 *mm* displacement, equivalent to 4.0% drift, in cycle 16

(f) at 100 *mm* displacement, equivalent to 5.0% drift, in cycle 18

(g) at 120 *mm* displacement, equivalent to 6.0% drift, in cycle 20

(h) at 140 *mm* displacement, equivalent to 7.0% drift, in cycle 22

(i) Stop loading

Fig. 10. Deformation of ELBRF specimen at different stages of displacement in laboratory test, [31].

(a) Start loading

(b) at 20 *mm* displacement, equivalent to 1.0% drift, in cycle 9

(c) at 40 *mm* displacement, equivalent to 2.0% drift, in cycle 12

(d) at 60 *mm* displacement, equivalent to 3.0% drift, in cycle 14

(e) at 80 *mm* displacement, equivalent to 4.0% drift, in cycle 16

(f) at 100 *mm* displacement, equivalent to 5.0% drift, in cycle 18

(g) at 120 *mm* displacement, equivalent to 6.0% drift, in cycle 20

(h) at 140 *mm* displacement, equivalent to 7.0% drift, in cycle 22

(i) Stop loading

Fig. 11. Deformation of QXBRF specimen at different stages of displacement in laboratory test.

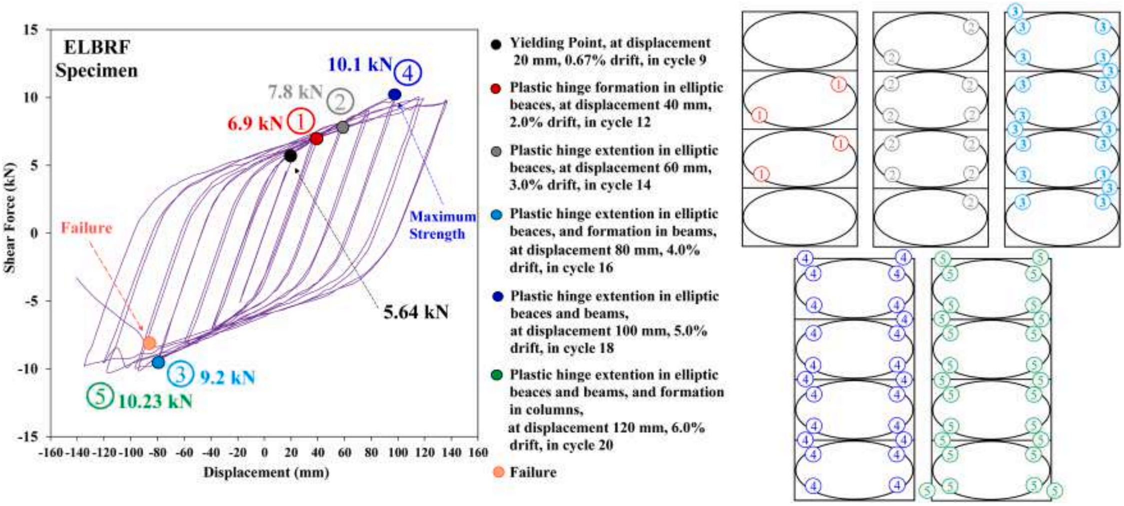

Fig. 12. Experimental hysteresis curves and plastic hinge formulation in ELBRF specimen.

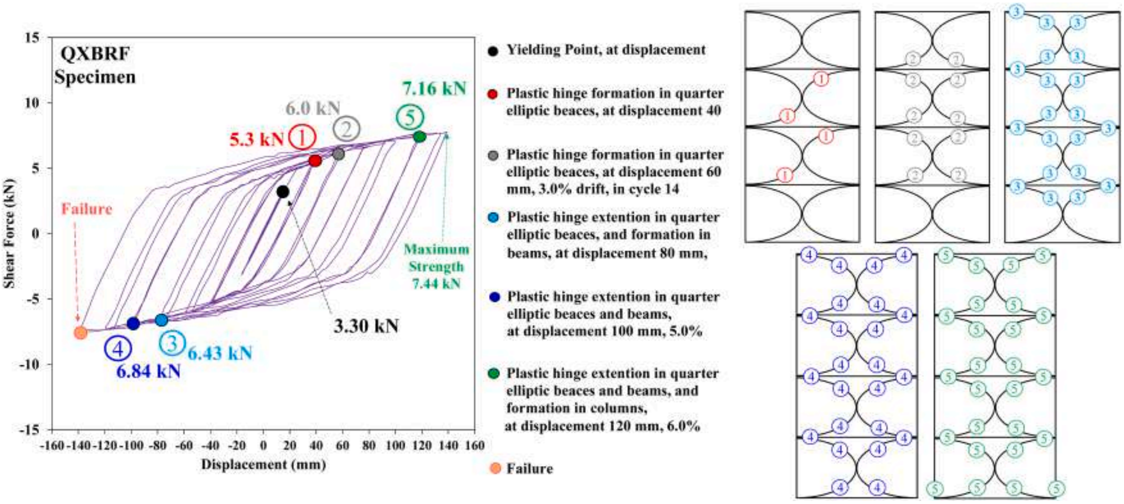

Fig. 13. Experimental hysteresis curves and plastic hinge formulation in QXBRF specimen.

2. **Post-Yielding Stage:** This stage follows the yielding point, where the material begins to deform plastically, showing a non-linear behavior where the structure does not fully recover after the load is removed.
3. **Strength Degradation Stage:** As the cyclic loading continues, the capacity of the structure to withstand further load decreases, indicating damage accumulation and the onset of failure mechanisms.

These stages are distinctly observable in the backbone curve discussed in Section 4.4.

In the ELBRF test, during the first nine loading cycles, the structure demonstrated elastic behavior, with the deformations of the elliptic braces being reversible. The shear strength of the specimen at displacements of 13.4 *mm* and 20 *mm*, corresponding to 0.67% and 1.0% drift, was 3.1 kN and 5.64 kN, respectively. The lateral resistance of the specimen increases after yielding, and hardening is observed in the hysteresis curve. The resistance peaked at 7.8 kN, 9.2 kN, and 10.1 kN for displacements of 60 *mm*, 80 *mm*, and 100 *mm*, corresponding to drift percentages of 3.0%, 4.0%, and 5.0%, respectively. This resistance then stabilized with a minor increase up to a drift of 6%. The test stopped at the 22nd cycle, where the shear capacity was measured at 9.78 kN during loading, as shown in Fig. 12.

In the QXBRF test, the specimen remained elastic during the first six cycles at approximately 0.67% drift, with a shear strength of 4.24 kN at a displacement of 20 *mm*, equivalent to 1.0% drift. The lateral resistance of the specimen increased to 5.29 kN, 6.0 kN, 6.43 kN, and 6.84 kN at 40 *mm*, 60 *mm*, 80 *mm*, and 100 *mm* displacements, corresponding to 2%, 3.0%, 4%, and 5.0% drifts, respectively, and continued to increase slightly until the end of cyclic loading. The test stopped at the 22nd cycle, with a recorded shear capacity of 6.84 kN during loading (Fig. 13).

The quarter-elliptic braces of both the ELBRF and QXBRF specimens exhibit a marked reduction in stiffness after yielding due to the development of plastic hinges. This leads to a decline in specimen strength as wrinkling occurs and additional plastic hinges form on both the braces and columns, particularly evident at the end of the test. Hysteresis curves from these tests offer insights into aspects like strength, stiffness, ductility, overstrength, energy dissipation, damping efficiency, seismic performance metrics, and the progressive decline in strength and stiffness. The curves for both specimens reveal three clear phases: elastic, post-yielding, and strength degradation, which are distinctly depicted in the backbone curve analyzed in Section 4.4.

The ELBRF specimen exhibited compressive loads of 5.1 kN, 6.78 kN, 7.72 kN, and 9.11 kN at drift levels of 1%, 2%, 3%, and 4%, while the QXBRF experienced loads of 4.50 kN, 5.26 kN, 5.8 kN, and 6.31 kN at these drifts. Under tension, the ELBRF maintained loads of 5.2 kN, 6.9 kN, 7.8 kN, and 9.2 kN from 1% to 4% drift, and the QXBRF managed

4.24 kN, 5.29 kN, 6.0 kN, and 6.43 kN. The maximum compressive loads reached 10.1 kN for the ELBRF and 7.44 kN for the QXBRF, with peak tensile loads at 10.23 kN and 7.48 kN, respectively. In the last cycles of the QXBRF's hysteresis curve, a minor increase in the maximum compressive load occurred, as seen in Fig. 13. The test ended due to widespread plastic hinges in both brace types across all stories, as well as in the beams and columns.

4.3. *Cyclic energy*

Inelastic deformations in structural components under cyclic loading lead to hysteretic energy dissipation, which is quantified by the area under the force-displacement curve obtained from the cyclic tests. Fig. 14 shows the energy absorbed during each cycle and the cumulative dissipated energy for both the ELBRF and QXBRF systems. Key observations from the energy curves for each specimen are presented.

The area under the hysteresis curve represents the energy dissipated in the structure during processes such as steel yielding, crack opening and closing, weld deformation, and bolt loosening. Energy is stored and dissipated during each cycle within each hysteresis loop. For the ELBRF system, the cumulative dissipated energy was 17,549 J, while for the QXBRF system, it was 13,925 J. Notably, ELBRF dissipated 27.6% more energy than QXBRF. The first bar in the bar chart marks the start of the first plastic cycle, where energy dissipation is initially considered zero, as the load-displacement curve in the first cycle is a straight line with no area. In the ELBRF, energy dissipation increases uniformly for two cycles before reaching maximum strength, but then drops. After this drop, the energy dissipation process resumes. This drop could be due to a loss of strength. After the cycle with maximum strength, energy dissipation increases linearly and uniformly in the QXBRF, but the rate decreases after the cycle in which some connections fail. Observations of cyclic performance reveal that the curved geometry of the elliptic braces leads to a rapid transition from tensile to compressive forces in the quarter-elliptic braces during cyclic loading direction changes. This dynamic response prevents permanent deformations and out-of-plane buckling, emphasizing the importance of the quarter-elliptic braces' shape in enhancing energy dissipation in both the ELBRF and QXBRF systems.

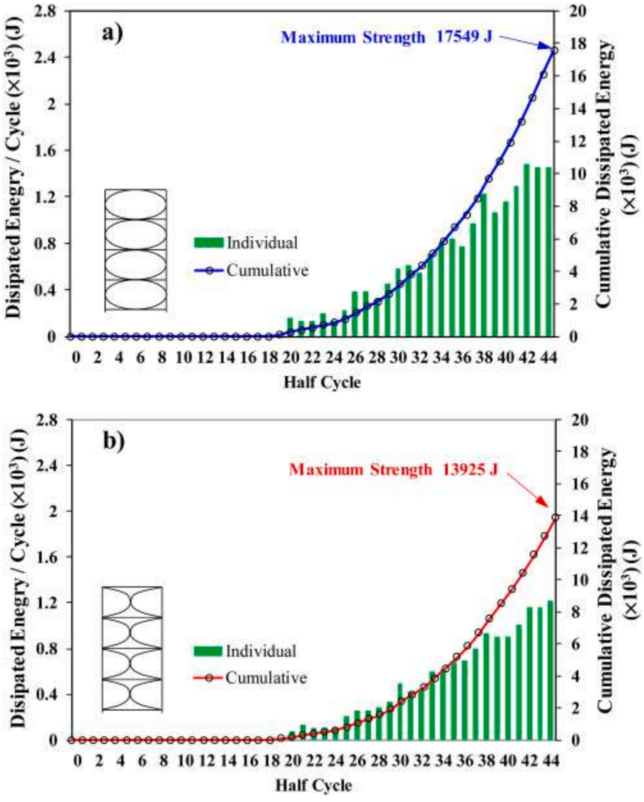

Fig. 14. Cumulative and cyclic dissipated energy in a) ELBRF and b) QXBRF.

4.4. *Backbone curve*

The backbone curve, derived from load-displacement cycles, serves as the pushover curve in the idealization process according to FEMA-356 [41]. The area under the nonlinear curve, referred to as the hysteresis curve, should match the area under the idealized curve. Fig. 15 illustrates both the hysteresis and backbone curves, along with key seismic parameters crucial for studying the structure's behavior. In Fig. 15, Δ_y, Δ_u, P_y, P_u, K_e, K_{py}, E_h, ξ_{hyst}, Ω, and μ represent the yield displacement, ultimate displacement, yield force, ultimate force, elastic stiffness, post-yield stiffness, dissipated energy, equivalent hysteresis damping coefficient, overstrength, and ductility factor, respectively.

The experimental backbone curves for the ELBRF and QXBRF in both the positive and negative loading regions are shown in Fig. 16. As observed, the ELBRF backbone curve is higher than that of the QXBRF, indicating that the ELBRF exhibits greater stiffness and strength compared to the QXBRF. The enhanced elastic stiffness of the ELBRF is attributed to the connection of the elliptic brace to the middle of the beams and columns, effectively restricting rotation at the beam-column connections and strengthening the frame. In contrast, in the QXBRF system, the elliptic brace intersects at the center of the moment frame, allowing more rotation at the beam-column connections due to the reduced bracing restriction. The distinct behavior of these two systems can be attributed to the connection of the elliptic braces and the inherent geometric properties of the braces.

Table 3 presents a summary of the yield displacement, ultimate displacement, yield strength, and ultimate strength for both systems. The yield displacements for ELBRF and QXBRF are 16.7 *mm* and 17.7 *mm*, respectively, indicating a negligible difference. However, the yield strength of ELBRF is significantly higher at 6.23 kN, compared to 3.30 kN for QXBRF, reflecting a 45.8% greater yield strength in ELBRF. Despite both systems utilizing braces with the same geometric properties and quarter-elliptic dimensions, this disparity underscores a notable difference in their structural performance. Similarly, the ultimate force recorded for ELBRF is 10.1 kN, while QXBRF achieves 7.0 kN, demonstrating that ELBRF exhibits a 45.8% higher ultimate strength. This substantial difference highlights the superior load-bearing capacity of ELBRF, attributed to its brace configuration and connection detailing, which enhance its overall structural efficiency under cyclic loading.

5.5. *Stiffness*

Structural stiffness plays a pivotal role in determining seismic performance and even the potential for lateral dynamic instability in structures. This study focuses on three key stiffness parameters: elastic

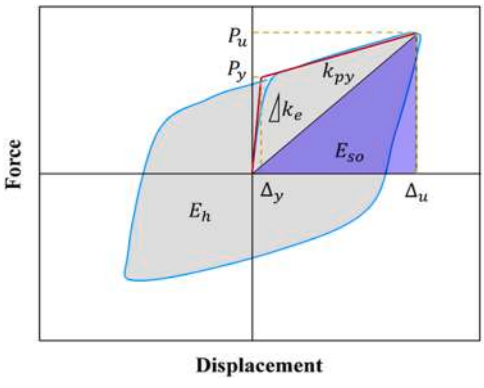

Fig. 15. Schematic representation of hysteresis parameters.

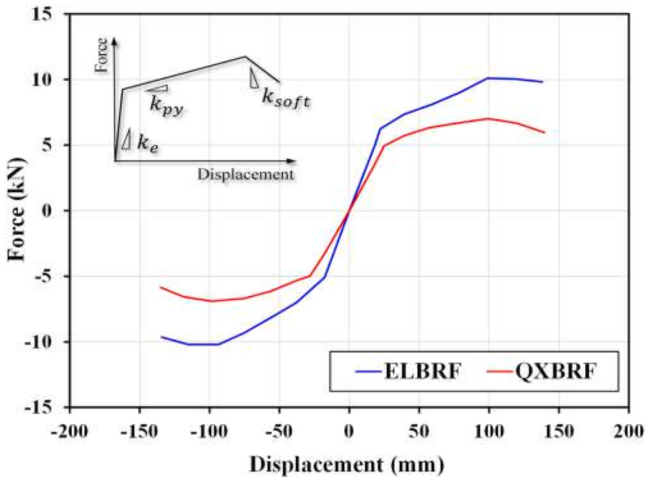

Fig. 16. Backbone curves for ELBRF and QXBRF specimen.

stiffness (K_e), post-buckling compressive stiffness (K_{py}), and softening stiffness (K_{soft}). These parameters are essential in shaping the structural response under seismic loads. The definitions of elastic stiffness, post-yielding stiffness, and softening stiffness are provided in Eqs. (1)–(3).

$$K_e = \frac{P_y}{\Delta_y} \tag{1}$$

$$K_{py} = \frac{P_u - P_y}{\Delta_u - \Delta_y} \tag{2}$$

$$K_{soft} = \frac{P_f - P_u}{\Delta_f - \Delta_u} \tag{3}$$

where P_f and Δ_f represent the failure strength and the corresponding displacement, respectively, a trilinear model was adopted to determine the elastic, post-yielding, and softening stiffnesses, as depicted in Fig. 16.

Elastic stiffness (K_e) is calculated from the initial portion of the load-displacement curve, prior to tensile yielding or compressive buckling in the bracing elements. This parameter is crucial for distributing lateral shear forces among the resisting members and for preventing non-structural damage under low-intensity loads such as wind or minor earthquakes. Post-buckling compressive stiffness (K_{py}), defined as the slope of the backbone curve following inelastic buckling, indicates the degree to which the structure's load-bearing capacity diminishes. It reflects the system's response under progressive inelastic deformation. Softening stiffness (K_{soft}) emerges after the structure reaches its maximum strength and begins to lose capacity due to the development of extensive plastic hinges and both local and global buckling in its members. Unlike the other stiffness parameters, softening stiffness is inherently negative. Both post-yielding and softening stiffness are critical indicators of the structural behavior after yielding. They offer insight into the system's hardening and softening characteristics and serve as valuable criteria for performance-based seismic design and assessment.

Table 4 summarizes the calculated values of elastic stiffness (K_e), post-yielding stiffness (K_{py}), and softening stiffness (K_{soft}), determined using Eqs. (1)–(3). The elastic stiffness of ELBRF is 447 N/mm, compared to 312 N/mm for QXBRF, showing a 43.2% higher stiffness for ELBRF. This disparity primarily stems from differences in brace design and the connection methods used to attach the elliptic quadrants to the frame, underscoring the importance of these factors in enhancing ELBRF's elastic stiffness.

Post-yielding stiffness (K_{py}) values for ELBRF and QXBRF are 27.2 N/mm and 20.0 N/mm, respectively, with ELBRF exhibiting a 36.1% higher value. Although this initial disparity in stiffness is significant, the gap narrows after yielding as plastic hinges form, reducing the difference in stiffness between the two systems. While the higher elastic stiffness of ELBRF is primarily due to the brace configuration and connections, the post-yielding stiffness difference diminishes as the frames enter the inelastic range.

Softening stiffness (K_{soft}) values, which characterize the system's behavior beyond maximum strength, are –10.3 N/mm for ELBRF and –27.4 N/mm for QXBRF. The negative values indicate a reversed slope on the backbone curve. QXBRF exhibits a steeper slope in the softening phase, primarily due to the development of cracks and ruptures in connection welds following peak strength. This degradation results in greater stiffness loss in QXBRF's hysteresis cycles compared to ELBRF.

4.6. *Seismic performance factors*

Seismic performance factors such as the ductility factor (μ), overstrength (Ω_o), and the response modification factor (R) were assessed for both the ELBRF and QXBRF systems based on experimental results and the methodology outlined in FEMA-356 [41]. As discussed in Section 4.4, the backbone curve is derived from the hysteresis data. As per FEMA-356 [41], only the ascending part of the hysteresis curve is considered to produce an equivalent bilinear curve; the descending part is disregarded, as depicted in Fig. 17.

In Fig. 17, point *B* is determined such that the length of line segment *AD* is 0.6 times that of *AB*, ensuring the intersection of the backbone curve with the initial segment of the bilinear curve corresponds to $0.6V_y$ (where Vy is the yield force). Furthermore, the area under the backbone curve is made equal to that under the idealized bilinear curve, yielding a simplified yet accurate representation of the structural response under seismic loading.

The response modification factor (R) plays a vital role in seismic

Table 3
Backbone results for specimens.

Specimens	$P_y(kN)$			P_u (kN)			$\delta_y(mm)$			δ_u (mm)		
	Pos.	Neg.	Avg.	Pos.	Neg.	Avg.	Pos.	Neg.	Avg.	Pos.	Neg.	Avg.
ELBRF	6.20	5.08	5.64	10.10	10.20	10.15	16.73	16.52	16.62	98.90	95.66	97.28
QXBRF	5.55	5.45	5.50	7.01	6.91	6.96	17.22	18.07	17.65	139.52	135.15	137.34

Table 4
Elastic, post-yielding and softening stiffnesses for specimens.

Specimen	K_e(N /mm)			K_{py}(N /mm)			K_{seft}(N /mm)		
	Pos.	Neg.	Avg.	Pos.	Neg.	Avg.	Pos.	Neg.	Avg.
ELBRF	435.48	458.45	446.97	26.79	27.54	27.17	-7.02	-13.58	-10.30
QXBRF	322.30	301.60	311.95	17.84	18.10	17.97	-26.17	-28.64	-27.41

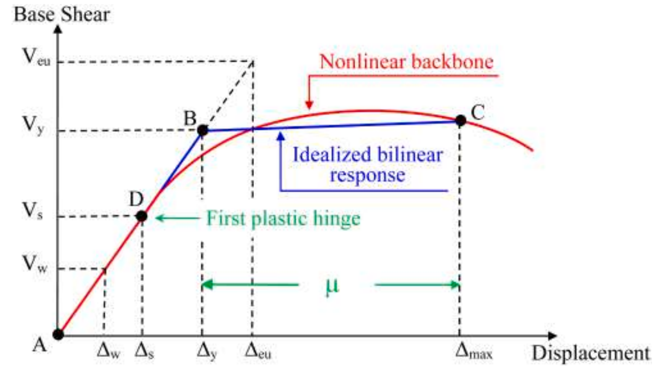

Fig. 17. Bilinear curve and test backbone in Uang's method.

design, capturing the essence of a structure's ductility and overstrength by simplifying its nonlinear behavior into that of an equivalent linear system. Since both ELBRF and QXBRF are novel structural systems, their R values are not yet included in existing seismic design codes. Therefore, the R values for these systems are calculated using the Uang method [42], which is represented by the equation below:

$$R_{LRFD} = \frac{V_{eu}}{V_s} = \frac{V_{eu}}{V_y} \times \frac{V_y}{V_s} = R_\mu \Omega_\circ \tag{4}$$

R is a key parameter in seismic design, representing a structure's ductility and overstrength by approximating its nonlinear behavior with that of an equivalent linear system. Since ELBRF and QXBRF are innovative systems, their R values are not currently included in existing seismic design codes.

The ductility factor (μ) is defined as the ratio of the maximum horizontal displacement (Δ_{max}) to the yield displacement (Δ_y). Similarly, the overstrength factor (Ω_o) is calculated as the ratio of the yield base shear (V_y) to the base shear at the onset of the first plastic hinge formation (V_s), following the methodology outlined by Uang et al. [42]:

$$\mu = \frac{\Delta_{max}}{\Delta_y} \tag{5}$$

$$\Omega_\circ = \frac{V_y}{V_s} \tag{6}$$

The period-dependent ductility factor (R_μ) represents the ratio of maximum elastic base shear (V_{eu}) to yield base shear (V_y), and it varies with the structure's vibration period (T). Due to differences in periods observed during repeated loading cycles in the frames, the smaller of the two calculated values $R_{\mu 1}$ and $R_{\mu 2}$ is used in determining the overall R-factor. In accordance with the method proposed by Newmark and Hall [43] method, R_μ is determined using the following equation:

$$\begin{cases} R_{\mu 1} = \sqrt{2\mu - 1} & ; \quad T < 1s \\ R_{\mu 2} = \mu & ; \quad T \geq 1s \end{cases} \tag{7}$$

Consequently, in accordance with [44,45], the coefficient of equivalent hysteresis damping, ξ_{hyst}, is expressed in the following equation:

$$\xi_{hyst} = \frac{E_h}{4\pi E_{so}} = \frac{A_{loop}}{2\pi V_m \Delta_m} \tag{8}$$

where E_h, E_{so}, V_m, and Δ_m represent the hysteretic damping or the dissipated energy in each cycle, the area of potential energy stored in a linearly elastic system with effective stiffness)K_{eff}(under elastic loading conditions, the average of maximum force (push-pull), and the average of the maximum displacement (push-pull) in the force-displacement curve.

Table 5 summarizes the seismic performance factors and the equivalent hysteresis damping coefficients for both the ELBRF and QXBRF systems. At the final limit state, the equivalent hysteresis damping coefficient was calculated as 17% for ELBRF and 23% for QXBRF. Despite ELBRF dissipating 26% more energy than QXBRF, it exhibited a lower damping coefficient. This suggests an inverse relationship between structural strength and the equivalent hysteresis damping coefficient within the same hysteresis loop. The response modification factors (R) for the ELBRF and QXBRF systems were determined to be 7.3 and 6.8, respectively. The ductility factors (μ) were 5.75 for ELBRF and 6.8 for QXBRF, while the overstrength factors (Ω_o) were 2.5 and 1.80, respectively.

4.7. *Cyclic strength degradation ratio*

The Cyclic Strength Degradation (CSD) ratio was utilized to evaluate strength degradation after yielding, focusing on hysteresis behavior and strength deterioration under cyclic loading. While this approach is similar to the method proposed by Chiniforush et al. [46], it involves slight differences in the calculation process. In this method, the force value of the last cycle at a specific force level, P_{cyc}, is divided by the corresponding value from the first cycle, P_{1c}. The ratio for each load level is determined using Eq. (9) and depicted in Fig. 18. During cyclic loading, plastic strains develop in the member, leading to the formation of plastic hinges that contribute to strength reduction. This ratio effectively identifies the onset, trend, and magnitude of strength degradation throughout cyclic loading.

$$CSD = \frac{P_{cyc}}{P_{1c}} \tag{9}$$

In ELBRF, the cyclic force ratio remained relatively stable after the yield displacement, except for the last two force levels, with some hardening observed at displacements of 40, 80, and 100 *mm*. However, the strength on the negative side dropped below the CSD = 1.0 line during the last two force levels, at displacements of 120 and 140 *mm*. For these final two cycles, the CSD ratios were 0.94 and 0.85, respectively. These ultimate force levels corresponded to two complete reversed cycles, characterized by brace wrinkling and extended plastic hinges in the members.

In contrast, QXBRF showed hardening at several force levels, but significant strength degradation occurred at the last two force levels. At the final displacement of 140 mm, the CSD ratios were 0.89 on the negative side and 0.74 on the positive side. At earlier force levels, the average CSD ratio drop for both sides were 0.96. In the last two QXBRF force levels, which equated to four complete reversed cycles, weld fractures were observed at the brace-to-column connection, along with plastic hinge formation in the brace members.

5. Failure mechanisms of specimens

5.1. *ELBRF specimen*

The deformation behavior of the elliptic braced frame under various stages of lateral loading is illustrated in Fig. 19. At low displacement levels, ranging from 0.33 to 0.67 times the yield displacement (δ_y), as

Table 5
The seismic performance factors and the coefficient of equivalent hysteresis damping of the ELBRF and QXBRF systems.

Specimens	Δy (mm)	Vy (kN)	μ	Ω_0	Cumulative E_h ($\times 10^3$ J)	ξ_{hyst} (%)	$R_{(LRFD)}$
ELBRF	16.62	5.64	5.75	2.5	17.55	17.01	7.30
QXBRF	17.65	5.50	6.79	1.78	13.92	23.14	6.78

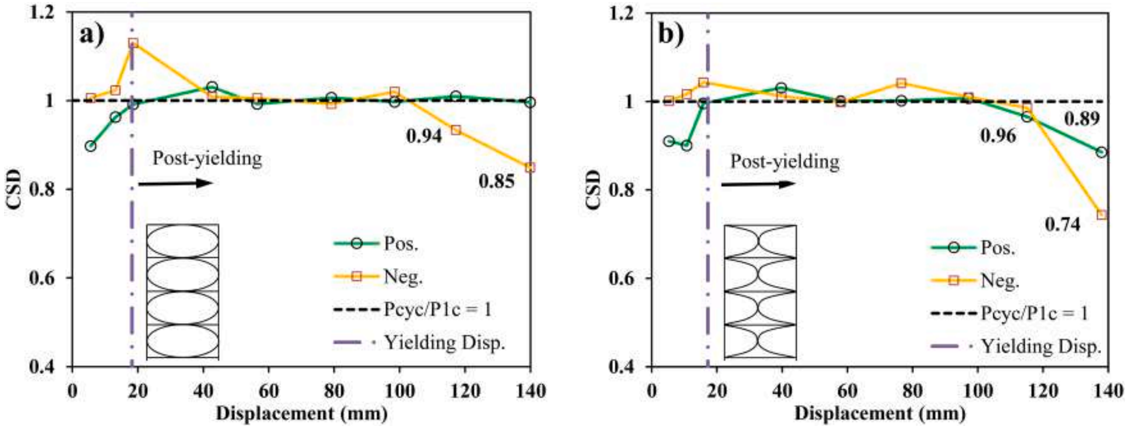

Fig. 18. Cyclic strength degradation ratio for a) ELBRF and b) QXBRF.

shown in Fig. 19(a), the frame undergoes negligible deformation. Upon reaching the yield drift (δ_y), depicted in Fig. 19(b), minor plastic deformation becomes visible in the elliptic braces, along with slight discoloration. The braces deform from an elliptic to a rectangular shape under loading but return to their original form during cyclic unloading. These deformations primarily occur in the braces and columns, while the beams remain unaffected after completing nine full loading cycles.

A more detailed explanation of the yielding process is presented in the strain gauge analysis section. Beyond the yield displacement, brace yielding becomes more pronounced. The frame shows the capacity to endure large plastic deformations even after 22 cycles, with displacement levels ranging from 4 to 7 times δ_y, as illustrated in Fig. 19(c and d). In the final state, the frame exhibits significant deformation and wrinkling in the braces, accompanied by plastic deformations in both beams and columns.

It is important to highlight that the overall condition of the columns and beams remained stable beyond the yielding displacement, with no significant buckling or fractures observed in the welds at the beam-to-column or elliptic brace-to-beam and column connections. The use of an auxiliary plate for welding the elliptic braces to the beams and columns [23–25,27] effectively prevented fractures at these joints. Nevertheless, some plastic deformations developed above the connections during the final loading stages.

In Fig. 20, the braces exhibit visible wrinkling, with hinge formations along their inner faces. These hinges developed during cyclic loading, leading to the transformation of the elliptic shape into a more rectangular form. Buckling initiated at displacements corresponding to δ_y, and wrinkling became prominent at displacements between 5 and 6 δ_y. The hinge locations are symmetrically distributed with respect to both the minor and major axes, as illustrated in Fig. 20.

Fig. 21 illustrates the plastic deformations at the elliptic brace-to-column connections at a displacement level of $7\delta_y$. The column and brace are welded to an auxiliary plate, which facilitates connection fabrication, prevents stress concentration in the welds, enhances rotational stiffness in the connection zone, and helps avoid the formation of plastic hinges in the column. No wrinkling or tearing is observed in the braces, although the upper portion of the auxiliary plate appears pale. This auxiliary plate significantly contributes to the stiffness of the connection, limiting rotation and thereby reducing local deformations. Since the frame's base beam is fixed to a base plate and undergoes minimal rotation, the lower half of the elliptic brace also exhibits limited rotational movement, with no paling observed in the lower region of the auxiliary plate, as shown in Fig. 21. At $7\delta_y$, some localized plastic deformations are visible on both sides of the auxiliary plate, particularly at the second, third, and fourth stories.

Fig. 22 shows the plastic deformations near the elliptic brace-to-beam connections across different stories. No paling is observed around the auxiliary plate in the connection zone at the bottom. In the first story, two small plastic deformations are visible in the upper and lower parts of the beam. In the second story, three plastic deformations are evident. Although plastic deformations in the third story could not be recorded due to the lateral restraint beam obstructing the view, it was confirmed that no plastic deformation occurred in this region. No plastic deformations are observed around the auxiliary plate in the fourth story. More significant changes are noted at the connections in the beams of the first and second stories. The auxiliary plates help avoid stress concentration in the column, redirecting plastic deformations from the column to the elliptic braces. The number and severity of plastic deformations in the auxiliary plates of the beams are less than those observed in the auxiliary plates of the columns. These observations, made at $7\delta_y$, represent a substantial displacement compared to traditional lateral load-bearing systems like CBFs. This behavior is attributed to the system's high ductility, adequate lateral strength, and appropriate stiffness, as shown in prior studies [21,23–25].

In the course of the examination, three distinct types of deformation failures were observed in the elliptic braces: local buckling, wrinkling, and tearing. These types of failures are commonly encountered when steel boxes are bent using methods such as Rotary-Draw Bending (RDB) and Three-Point-Roll Bending (TPRB) [47–49]. The failures are illustrated in Figs. 23-25 during cyclic loading. At low force levels (where $\delta < \delta_y$), the compressive stresses on the brace exceed the critical buckling stress threshold of the box plates, leading to local buckling at specific sections, as shown in Fig. 23. As the force increases (where $1 \sim 2\delta_y < \delta$), the compressive stresses across the plate's cross-section intensify, causing the compressive face of the plate to wrinkle and undergo both nonlinear geometric and material deformations, depicted in Fig. 24. As the cycle count increases to $3 \sim 7\ \delta_y$, the stresses from low-amplitude fatigue in the section cause the plate to rupture, as shown in Fig. 25. Seismic loads, which induce significant plastic strains in plastic hinges, contribute to this low-amplitude fatigue [50,51]. Observations show that wrinkling and tearing are predominantly seen in the middle of the elliptic braces, whereas local buckling occurs near the connection points and around the auxiliary plates.

5.2. QXBRF specimen

Fig. 26 illustrates the deformation stages of the QXBRF at displacements of δ_y, $2\delta_y$, $4\delta_y$, and $7\delta_y$. These larger displacements, exceeding $2\sim3\ \delta_y$, were documented to analyze the structural behavior and identify failure mechanisms of the frame. During cycles with displacements of 0.33 δ_y and 0.67 δ_y, no plastic deformations were observed, and the frame's response remained within the elastic range. The elliptic brace within the frame reverted from its original shape to a deformed state and back to its original shape during these cycles. However, at displacement

Fig. 19. Deformations of ELBRF at different displacements; a) 0.67δ_y, b) δ_y, c) 4δ_y, and d) 7δ_y.

levels of δ_y, signs of paling on the braces were noted. By 2δ_y, these paling areas expanded, accompanied by plastic deformations in the central sections of the braces. At 3δ_y, some braces in the upper stories showed plastic deformations and wrinkles.

At 4δ_y, cracks and separations were detected in some of the welds connecting the braces to the columns, though this was limited to only one connection among the stories, with the others remaining undamaged. After reaching 5δ_y, the braces in the second and third stories exhibited complete wrinkling and deformation. In addition, cracks appeared in connections that were previously sound. By 6δ_y, and persisting to 6~7δ_y, a crack was found in the base plate connection. At this stage, most braces had undergone plastic deformation and wrinkling. The weld connecting the brace to the column also failed. The principal failure mechanism in this frame occurs at the connections between the brace, beam, and column, where significant tensile stresses are exerted on the connections.

The final state of frame deformation, as depicted in Fig. 27, reveals plastic deformations and wrinkling specifically on the second story. The formation of plastic hinges within the frame is asymmetric. On the left side, two plastic joints emerge in the middle section of the elliptic brace, whereas on the right side, a single plastic hinge forms near the connections of the elliptic brace.

Notably, no paling, deformation, or cracks were observed in the area where the auxiliary plate is welded to the elliptic connection zone. This lack of damage can be attributed to the vertical application of stresses on the auxiliary plate, which results in shear-type stresses on the weld. The absence of any cracking in this region suggests that the weld possesses adequate ductility and strength to handle the applied stresses.

Plastic deformation in the elliptic brace begins with the bending of the inner face of the brace, and as the deformation progresses, wrinkling becomes evident on the same inner face. Fig. 28 illustrates two types of these deformations: (a) and (b). Specifically, in Fig. 28 (b), two wrinkles

Fig. 20. Locations of Wrinkles and plastic deformations at 7δ_y.

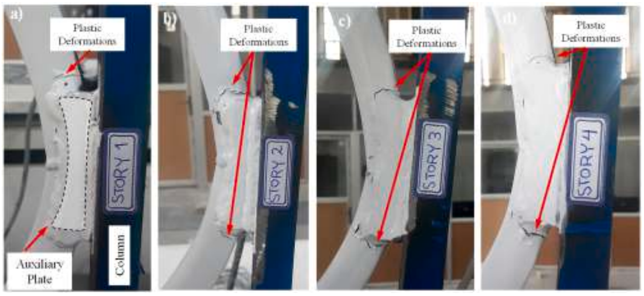

Fig. 21. Plastic deformations in elliptic brace-to-column connections at displacement 7δ_y: a) first story, b) second story, c) third story, and d) fourth story.

Fig. 22. Plastic deformations in elliptic brace-to-beam connections at drift 7δ_y a) base, b) first story, c) second story, d) third story, and e) fourth story.

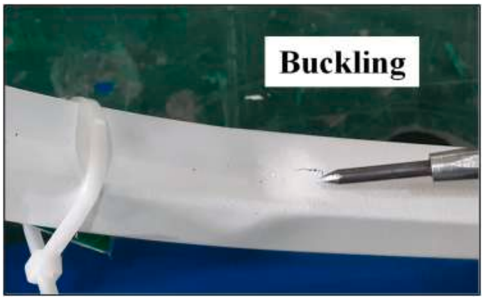

Fig. 23. Local buckling at elliptic braces at final status of specimen.

Fig. 24. Wrinkling at elliptic braces at final status of specimen.

Fig. 25. Tearing and rupture in the elliptic braces at final status of specimen.

appear in sequence, with the deformation in the right wrinkle being visibly more pronounced. Due to the significant tensile stresses at the weld location, cracks are observed in the Heat-Affected Zone (HAZ) at the Quasi-X brace-to-beam and column connections when displacements exceed 4δ_y, as shown in Fig. 28 (c). Finally, Fig. 28 (d) displays the fractured connection welds in their ultimate deformation state at 7δ_y, attributed to insufficient ductility in the transverse welding of the connections [52,53].

5.3. Specimen's strain

Strain gauges were placed on the columns and braces of both the ELBRF (Elastic Link Brace Frame) and QXBRF (Quasi-X Brace Frame) to monitor the onset of yielding and measure strains under cyclic loading conditions. These strains result from the combined effects of bending and axial forces experienced during the loading cycles, with the objective of pinpointing potential locations for plastic hinge formation. Figs. 29–32 display the strain data for ELBRF and QXBRF. In these figures, the vertical axis represents strain, while the horizontal axis indicates the number of loading cycles. Two horizontal lines on each curve signify the yield strain thresholds for the materials used in the columns and braces, providing a reference for assessing when the material begins to yield under the applied loads.

The strain patterns in the column of the ELBRF exhibited a zig-zag, nearly symmetric behavior, with most cycles up to the 22nd cycle remaining within the elastic strain range. However, both the 22nd and 23rd cycles exceeded these elastic limits. In contrast, the strains in the braces predominantly remained positive and did not revert to negative values, suggesting that these braces were subjected to continuous tension rather than returning to compression. It was observed that most

Fig. 26. Deformations of QXBRF at different displacements; a) 0.67δ_y, b) δ_y, c) 4δ_y, and d) 7δ_y.

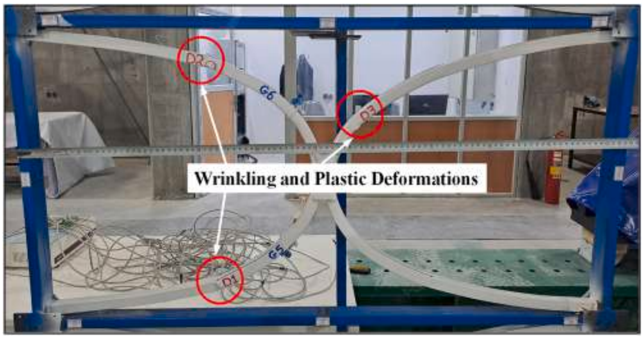

Fig. 27. Locations of Wrinkles and plastic deformations at 7δ_y.

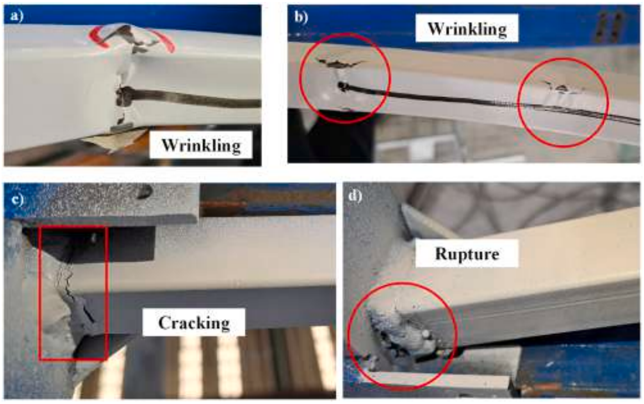

Fig. 28. Deformations and failure in the QXBRF, a and b) Wrinkling, c) cracking in the weld, and d) rupture in weld at the final status of specimen.

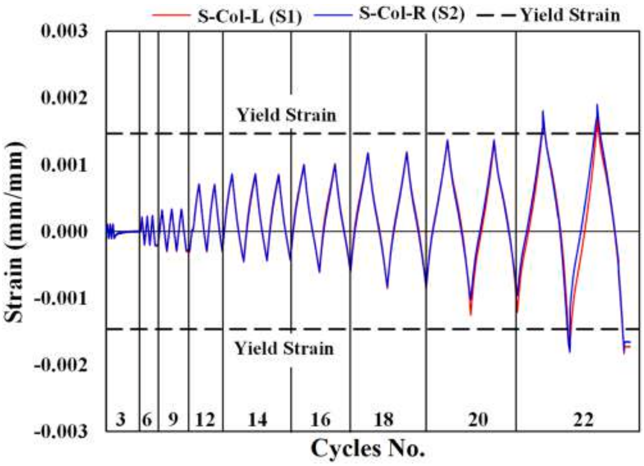

Fig. 29. History of strain in left and right columns of ELBRF.

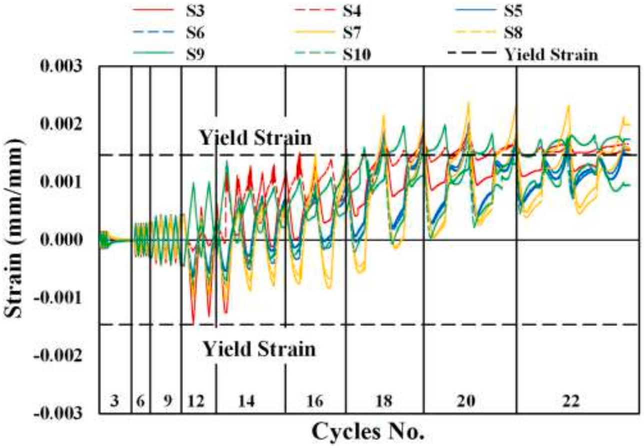

Fig. 30. History of strain in braces of ELBRF.

points along the braces had undergone yielding, which was confirmed by the failure modes, where plastic hinges formed in all braces. These plastic hinges in the braces yielded in fewer cycles compared to the column, demonstrating the system's capacity to absorb and dissipate energy from cyclic loading. This indicates that the braces are more susceptible to yielding, thus playing a critical role in energy dissipation within the structure.

At the 18th loading cycle, the column of the QXBRF began to yield. Despite this, after six additional cycles, the column continued to bear loads at strains beyond the yield point. Although the column entered an inelastic state, there were no indications of either local or global buckling, and no rupture occurred in the column despite its inelastic behavior over these cycles. The strain patterns in the braces of the QXBRF followed a trend similar to that of the columns but were not symmetrical. The amplitude of strain variation was more significant in this specimen compared to the ELBRF, with strains oscillating in both positive and negative directions. This suggests that the QXBRF experienced cyclic strains that surpassed the elastic limit in both tension and compression, unlike the ELBRF, where strains exceeded the elastic limit

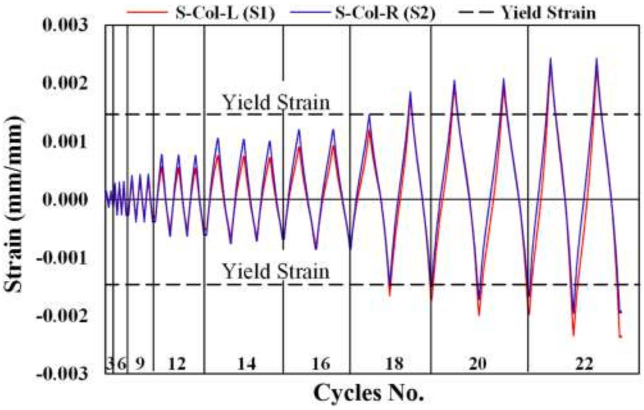

Fig. 31. History of strain in left and right columns of QXBRF.

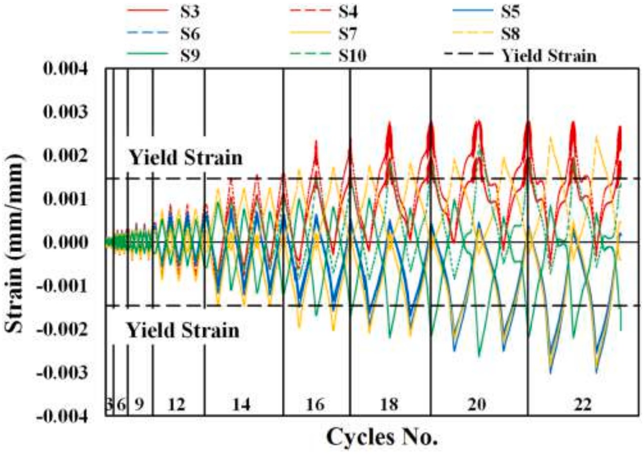

Fig. 32. History of strain in quarter-elliptic braces of QXBRF.

only in the positive (tension) direction.

Table 6 presents data on the yield cycle, direction of yielding, and maximum strain for both the ELBRF and QXBRF, covering all strain gauges. The yield strains for brace and column members are specified as 0.001465 and 0.001445, respectively.

For the ELBRF:

1. The first yielding occurred at position S-3 on the first story
2. Subsequently, S-4 and S-7 yielded on the second and third stories, respectively.
3. On the second, third, and fourth stories, S-10, S-5, S-6, S-8, and S-9 yielded nearly simultaneously, all after the 16th cycle. This indicates a uniform distribution of yield strains across the stories.
4. The column bases yielded at cycle 22, after the braces, which is indicative of an effective failure sequence in seismic-resistant systems.

For the QXBRF:

1. The first yield position was S-3, similar to the ELBRF, but it was accompanied by S-7 on the third story, yielding simultaneously.
2. At cycle 16, braces at S-4, S-5, S-8, and S-10 across all stories yielded.
3. Positions S-9 and S-6 were the last to yield among the braces.
4. The columns yielded in conjunction with S-6 on the second story.
5. The column in the QXBRF yielded at cycle 18, earlier than in the ELBRF (cycle 22), but it still managed to withstand 18 cycles of lateral loading.

This data suggests that while the QXBRF's column yielded earlier, it still demonstrated significant resilience against lateral loads, highlighting differences in the structural behavior and yielding patterns between the two frame types.

6. Behavior comparison of bracing systems

ELBRFs and QXBRFs offer unique benefits when compared to other bracing systems in steel structures. To assess these advantages, we conducted an extensive study focusing on the seismic performance, energy dissipation capabilities, and failure modes of both single-span, four-story ELBRF and QXBRF models, scaled at 1/6. These models underwent cyclic quasi-static testing, and their outcomes were compared for analysis.

To further understand the behavior of the proposed QXBRF, the results were benchmarked against those of X-braced frames at the base story, utilizing the dimensional details outlined in Fig. 4, through nonlinear FEM analyses. For an in-depth comparison, the designs of these frames were first established (refer to Table 7) before they were subjected to various loading scenarios using Abaqus software [38].

6.1. Modeling techniques

To further explore the behavior and perform a parametric study on the ELBRF, QXBRF systems, and X-braced frame, a Finite Element (FE) analysis was conducted using Abaqus software [38]. The analysis used the same geometric dimensions as those in the experimental models. All

Table 7
Numerical models sections.

Specimen	Beam section	Column section	Brace section
Elliptic braced frame	BOX 40×20×2	BOX 40×20×2	BOX 20×20×1
Quasi-X braced frame	BOX 40×20×2	BOX 40×20×2	BOX 20×20×1
X-braced frame	BOX 40×20×2	BOX 40×30×3	BOX 20×20×2.5

Table 6
Characteristics of strain in columns and braces.

Number of Story	Strain Gage No.	ELBRF				QXBRF			
		Loading Direction	Yield at Cycle No.	Number of Plastic Cycles	Max. Strain	Loading Direction	Yield at Cycle No.	Number of Plastic Cycles	Max. Strain
4	S-10	Pos.	17	7	0.00176	Pos.	16	8	0.00224
	S-9	Pos.	18	6	0.00199	Neg.	17	7	0.00263
3	S-8	Pos.	18	6	0.00191	Pos.	16	8	0.00244
	SG-7	Pos.	16	8	0.00129	Neg.	13	11	0.00288
2	SG-6	Pos.	18	6	0.00202	Neg.	18	6	0.00257
	SG-5	Pos.	18	6	0.00190	Neg.	16	8	0.00302
1	SG-4	Pos.	16	8	0.00176	Pos.	16	8	0.00290
	SG-3	Neg.	10	14	0.00184	Pos.	13	11	0.00281
Base	SG-Col-R	Pos.	22	2	0.00177	Pos.	18	6	0.00238
	SG-Col-L	Pos.	22	2	0.00190	Pos.	18	6	0.00243

parts of the structure were represented using the 3D 8-node linear brick element with reduced integration (C3D8R). During meshing, C3D8R elements (8-node linear brick elements with reduced integration) were selected to capture the elements of the frames in nonlinear behavior effectively. Curved braces, which are known to be the most sensitive components, were discretized with at least two elements through their thickness using the sweep meshing technique and the median axis algorithm. The mesh size for beams and columns is set to a maximum of 50 *mm*. On the other hand, due to the sensitivity and severity of plasticity for curved braces, the mesh size is set to 25 *mm*. In addition, mesh convergence study was performed on the finite element modeling with 10 different mesh sizes, and the best mesh size was considered for beam, column, and curved brace elements.

For enhanced accuracy and to address challenges such as global and local buckling, as well as shear locking, a detailed mesh was applied across all frame types. The analysis considered nonlinear geometry and large deformations by enabling the NlGeom option. Material characteristics, including the elastic modulus (E), yield stress (f_y), ultimate stress (f_u), and elongation, were obtained from tensile tests adhering to the ASTM A370 standard [36], with specifics listed in Table 2. A Poisson's ratio of 0.3 was uniformly applied to all materials. The cyclic behavior of the materials for the ELBRF, QXBRF, and X-braced frames was represented using the von Mises yield criterion alongside isotropic hardening rules. This study did not incorporate degradation from material fracture or steel tearing, focusing instead on the global behavior and failure modes of the structures.

Welds were modeled as part of a merged strategy within the simulation. While the experimental specimens used welded connections, the numerical model of this study employed tie constraints in Abaqus to simplify the analysis. This approach was taken because: (1) the study focused on global frame behavior rather than local weld effects, (2) it avoided complications from weld size scaling, and (3) the simplified model showed good agreement with experimental results.

Given the expected high plastic deformations and cyclic loading, a dynamic explicit method was chosen in Abaqus, with very small time increments to ensure accuracy in capturing the structural response. In the structural model, the base was constrained in all six degrees of freedom at the column's lowest level. A boundary condition was also applied at the third story to prevent out-of-plane movement ($u_z = 0$), simulating real-world conditions and ensuring structural integrity, Fig. 33.

During the experimental phase, cyclic loading was applied to the left side of the column according to the ATC-24 loading protocol, as detailed in the study's loading section. For the numerical simulations of the braced frames [54–56], accounting for initial geometric imperfections, which naturally occur in real-world structures, is essential. These imperfections were incorporated into the model via an Eigen analysis with a scaling factor of 0.0001, providing an accurate depiction of how the frame responds to loading. In ABAQUS, initial geometric imperfections are modeled by introducing deviations from the idealized geometry of a structure. This is typically done by applying an imperfection keyword, which can be used to modify nodal coordinates or define imperfection shapes based on buckling modes or previous static analysis results. These imperfections can significantly impact the buckling strength and stiffness of a structure, especially thin-walled members.

6.2. Numerical deformation under cyclic loading

Nonlinear finite element analyses were conducted on the ELBRF and QXBRF specimens at each stage of cyclic loading to validate their seismic performance and understand the failure mechanisms. The FEM was used to numerically evaluate stress and strain distributions, alongside the failure mechanisms, as the cyclic loading was applied to the test specimens. The significance of such studies lies in their ability to assess seismic behavior, identify vulnerabilities, explore failure mechanisms, and suggest retrofit strategies for structural seismic performance evaluation.

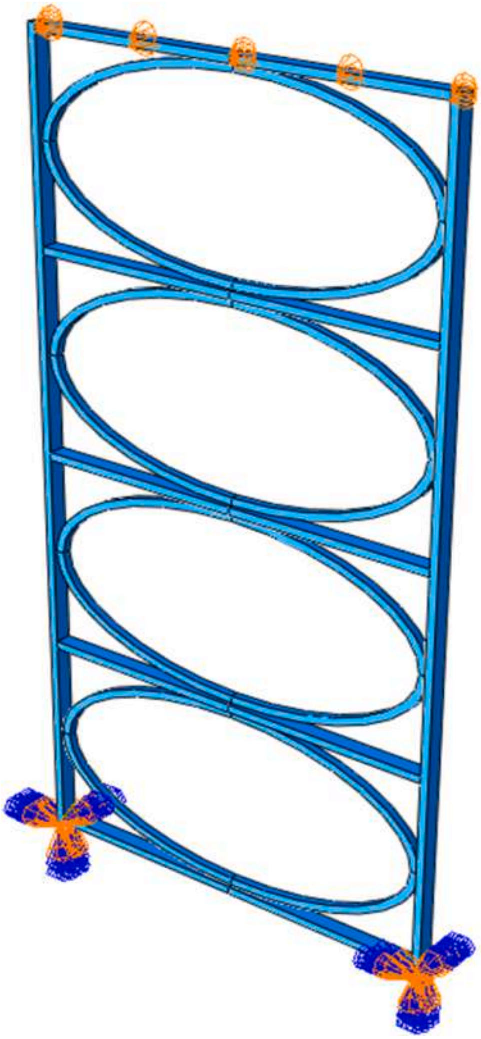

Fig. 33. Boundary conditions of the FE model in ELBRF.

Observations from these analyses at different loading stages include:

1. Initially, plastic hinges formed at the elliptic and quarter-elliptic braces with displacements up to 100 mm (5.0% drift).
2. As lateral forces increased, the progression of plastic hinges was observed first at the braces, then at both ends of the beams, and finally at both ends of the columns when displacement reached 140 mm (7.0% drift).

Von-Mises stress contours for the ELBRF and QXBRF at various cyclic loading stages are depicted in Figs. 34 and 35, respectively. These figures show:

1. No column buckling was observed in either system.
2. The elliptic and quarter-elliptic braces did not exhibit out-of-plane buckling throughout the loading up to 140 mm displacement.

The numerical results were found to correlate well with the experimental data for both ELBRF and QXBRF, as discussed in Sections 4.1 and 4.2. Figs. 34 and 35 also include comparisons of the lateral load-displacement curves from Abaqus simulations with those from the physical tests. Key aspects like maximum strength, elastic stiffness, post-yielding stiffness, and the hysteresis curve shape show good agreement with the test results. The average strength differences between the

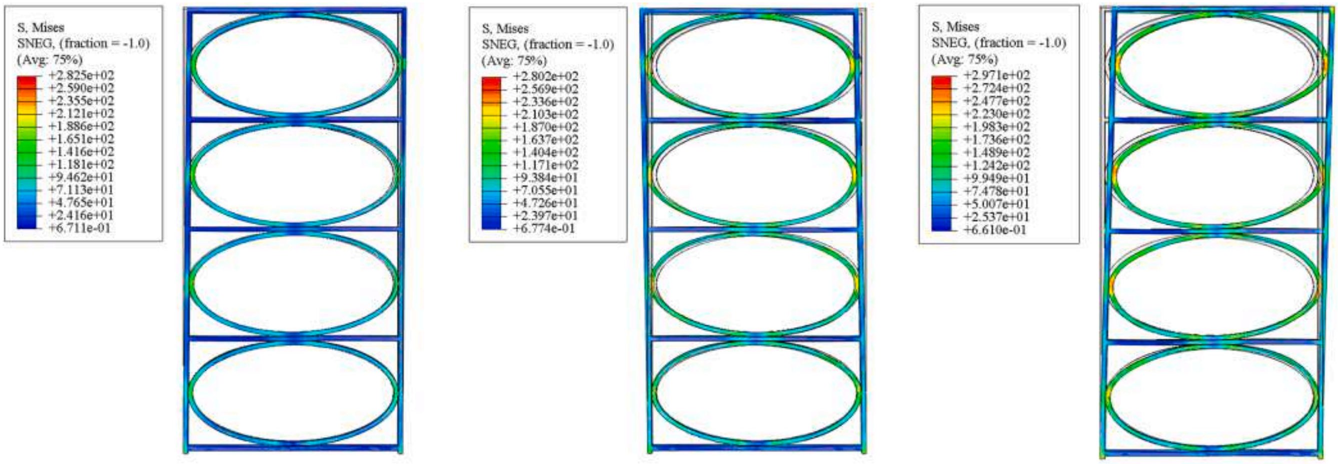

with 20 *mm* displacement, 1.0 % drift

with 40 *mm* displacement, 2.0 % drift

with 60 *mm* displacement, 3.0 % drift

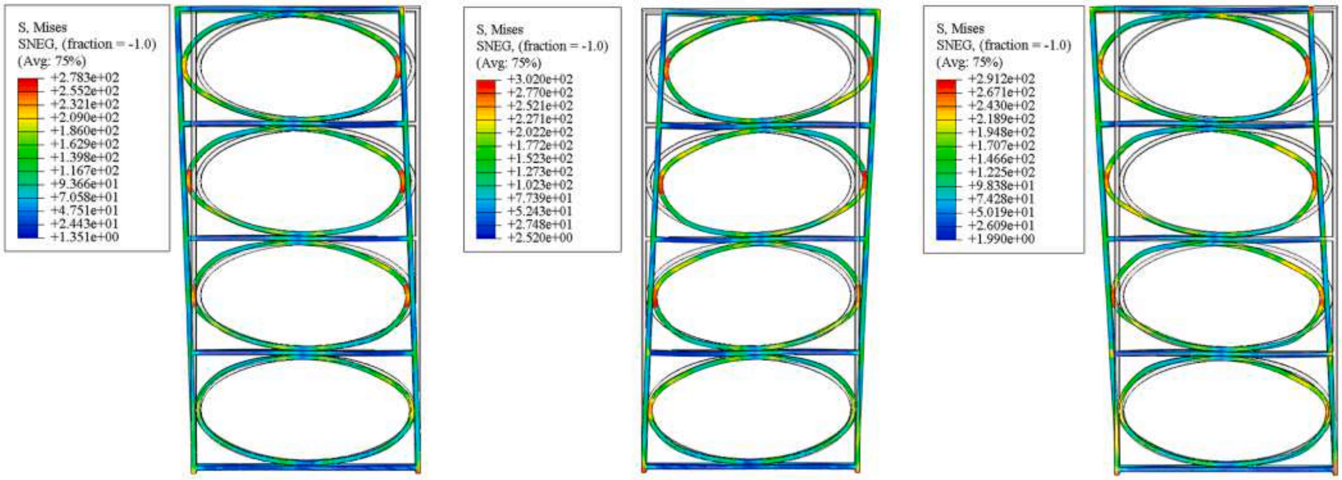

with 80 *mm* displacement, 4.0 % drift

with 100 *mm* displacement, 5.0 % drift

with 120 *mm* displacement, 6.0 % drift

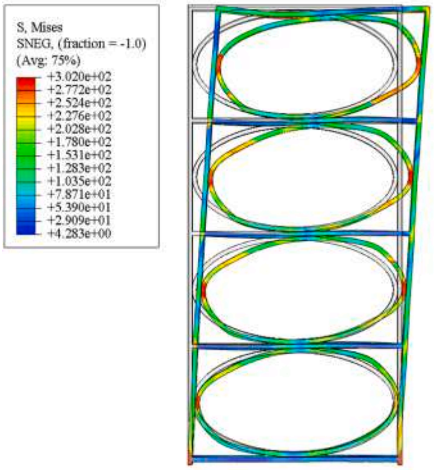

with 140 *mm* displacement, 7.0 % drift

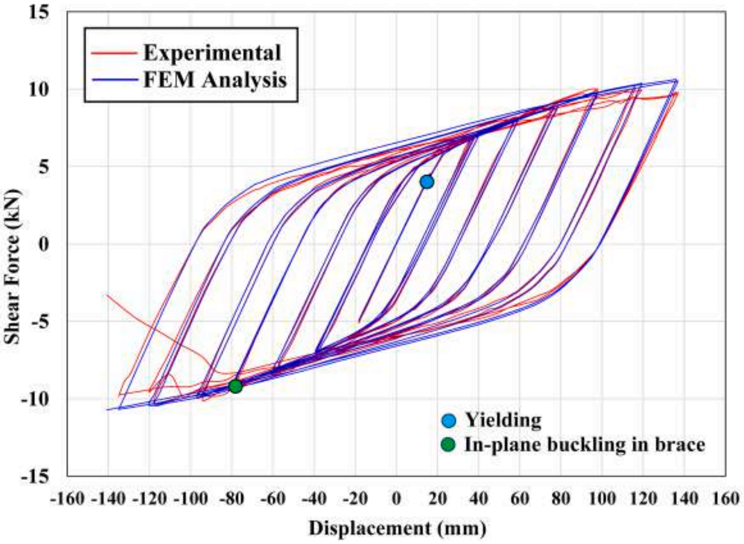

Fig. 34. Deformed shape and Von-Mises stress (Pa) in single-span four-story ELBRF specimen at different stages of cyclic loading [42].

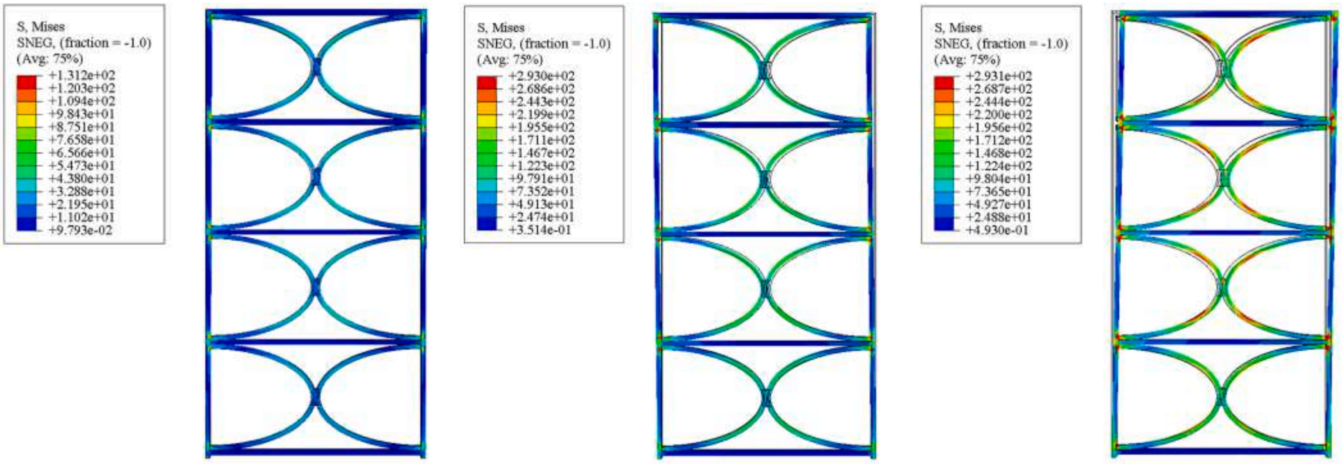

with 20 *mm* displacement, 1.0 % drift

with 40 *mm* displacement, 2.0 % drift

with 60 *mm* displacement, 3.0 % drift

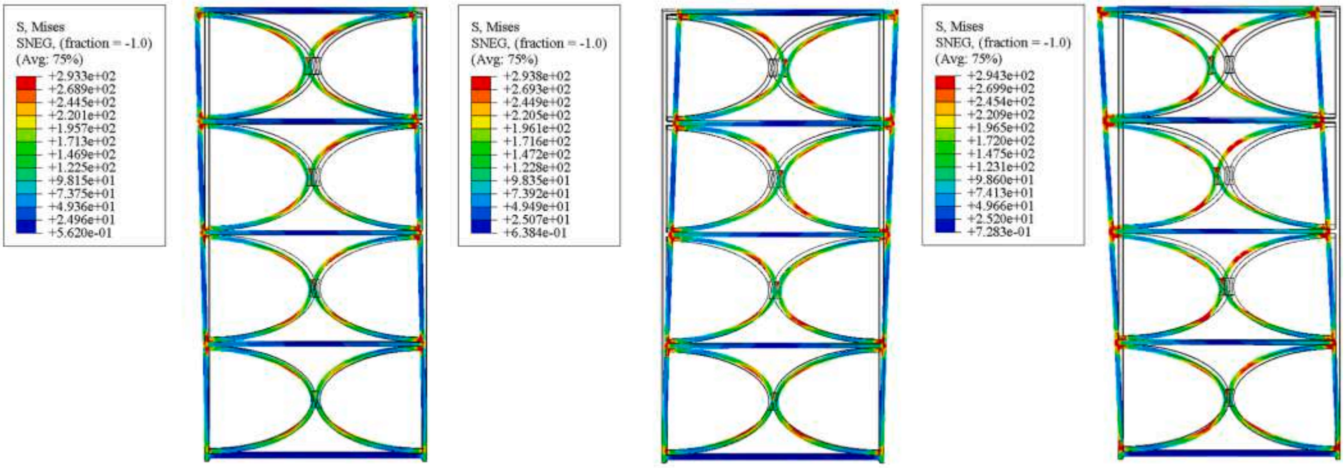

with 80 *mm* displacement, 4.0 % drift

with 100 *mm* displacement, 5.0 % drift

with 120 *mm* displacement, 6.0 % drift

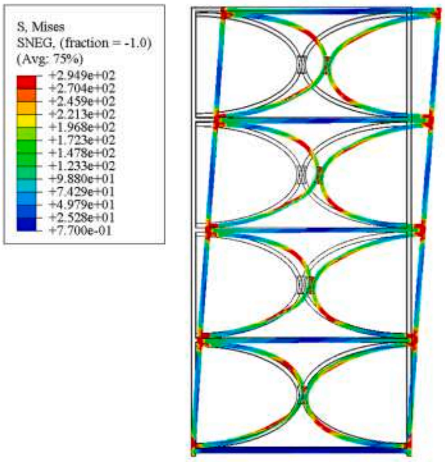

with 140 *mm* displacement, 7.0 % drift

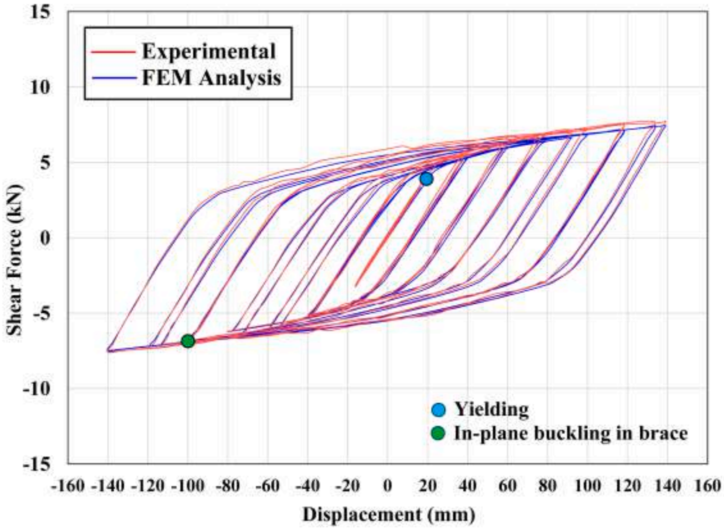

Fig. 35. Deformed shape and Von-Mises stress (Pa) in single-span four-story QXBRF specimen at different stages of cyclic loading.

numerical models and the experimental results were calculated at 5.01% for ELBRF and 6.54% for QXBRF, indicating a strong validation of the numerical models against the physical experiments.

As shown in Figs. 36 and 37, the Finite Element Method (FEM) provides an accurate prediction of the deformations observed at the final displacement stage. For the ELBRF, the deformations of the braces across various stories closely match those recorded in the physical test specimens. Additionally, the FEM accurately predicts the rotations at both ends of the story beams. For the QXBRF, the brace deformations also align well with the experimental observations. The unique positioning of the elliptic brace-to-beam and column connection at the corner of the specimen results in a notable reduction in the rotations of the beams, which the FEM model correctly captures. This demonstrates that the numerical simulations are reliable in predicting the structural behavior under the applied load conditions.

Eq. (10) describes the plastic strain equivalent (PEEQ) in Finite Element Method (FEM) modeling [38,57]. PEEQ serves as an effective measure for:

1. Identifying the locations where plastic failures occur.
2. Assessing the extent of plastic strains within the material.
3. Determining the onset of yielding.
4. Quantifying the values of plastic strains in the FEM model.

This criterion is particularly useful in understanding how materials behave under stress beyond their elastic limits, helping to predict and analyze plastic deformation and failure in structural components.

$$PEEQ = \int_0^t \sqrt{\frac{2}{3}\dot{\varepsilon}^{pl} : \dot{\varepsilon}^{pl}}\,dt \tag{10}$$

In tensor calculations, $\dot{\varepsilon}^{pl}$ represents the plastic strain rate, and the double dot product (:) denotes a contraction operation between two second-order tensors. For both the experimental and finite element analysis results, Fig. 38 shows the contours of Plastic Equivalent Effective Strain (PEEQ) on the inner face of the third-story elliptic brace in the ELBRF. The numerical model accurately identifies the location of the highest PEEQ, highlighting the region where plastic deformation is most pronounced.

Similarly, for the QXBRF, Fig. 39 displays the PEEQ contours on the top face of the brace. The numerical model accurately predicts the regions with the highest PEEQ values, indicating yielding. These areas, characterized by stress concentrations, are particularly evident on the inner face, where more pronounced color fading appears. This color change signifies higher plastic strain, and the model effectively represents this behavior, confirming its reliability in predicting plastic deformation and failure points in the structure.

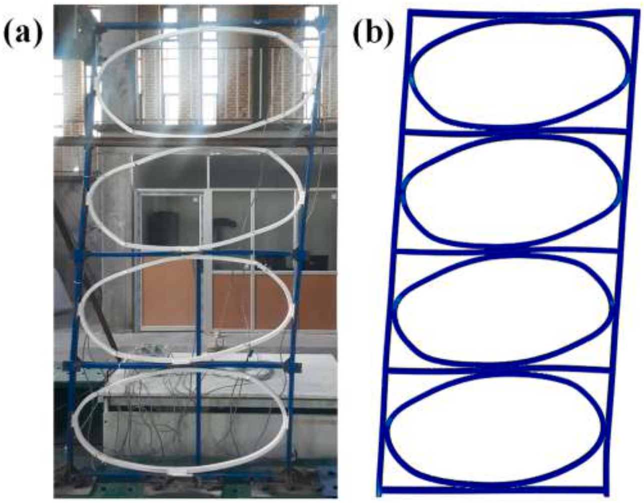

Fig. 36. Deformation for ELBRF at the final stage of cyclic loading: a) experimental test, and b) finite element analysis.

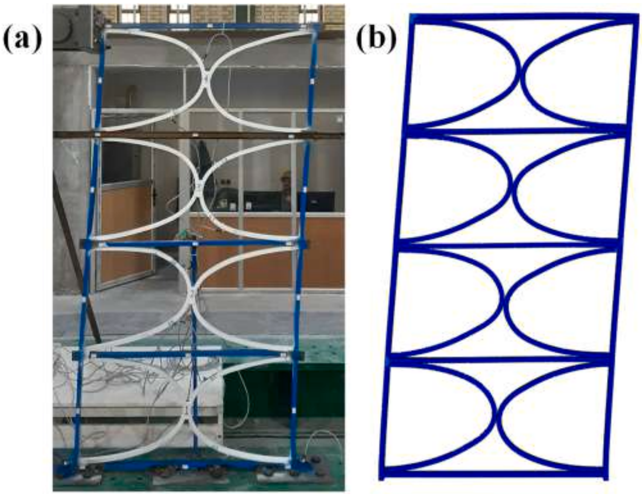

Fig. 37. Deformation for QXBRF at the final stage of cyclic loading: **a) experimental test, and b) finite element analysis.**

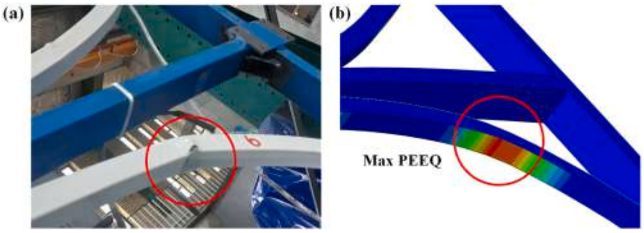

Fig. 38. PEEQ strain distribution for ELBRF at the final stage of cyclic loading: a) experimental test, and b) finite element analysis.

Below, the authors compare the seismic performance of the QXBRF specimen against that of an X-braced frame using a story-base model subjected to cyclic quasi-static loading. This comparison is based on the dimensional specifications provided in Table 7 and utilizes nonlinear FEM analyses.

1. In the QXBRF bracing system, no out-of-plane buckling of the quarter-elliptic braces was observed, even up to a displacement of 140 mm, as shown in Fig. 35. This indicates that the QXBRF exhibits higher resistance to deformation in this direction.
2. In contrast, for the X-bracing system, out-of-plane buckling of the braces occurred starting from a displacement of 20 mm, corresponding to a 1% drift, as shown in Fig. 40. This suggests that the X-braced frame is more susceptible to out-of-plane buckling under smaller displacements compared to the QXBRF design.

The Quasi-X bracing system, with its curved geometric configuration, experiences a distinct force distribution during cyclic quasi-static loading. This differs from traditional X-bracing in the following ways:

1. In the Quasi-X bracing system, as the direction of the lateral force changes, tensile forces in the elliptic braces are quickly followed by compressive forces. This rapid transition from tension to compression allows the quarter-elliptic elements under pressure to return to their original shape without permanent deformation. This characteristic helps prevent out-of-plane buckling, providing a significant advantage over conventional X-bracing.

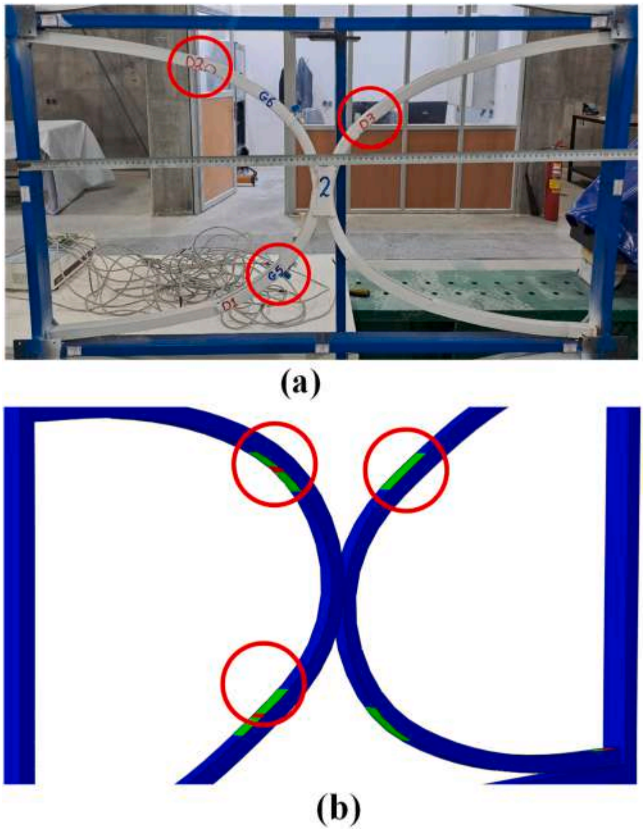

Fig. 39. PEEQ strain concentration for QXBRF at the final stage of cyclic loading: a) experimental test, and b) finite element analysis.

As shown in Fig. 35, this behavior reduces the risk of forming a first soft-story, enhancing overall building stability by mitigating hardening effects at large deformations in QXBRFs.

Conversely, the X-braced frame exhibits several drawbacks, as depicted in Fig. 40:

1. Shear failure occurs as tension braces yield and compression braces buckle out-of-plane, resulting in a significant decrease in strength, stiffness, and energy dissipation.
2. The asymmetry in brace behavior, with different responses in tension versus compression, causes damage to gusset plates and middle connections, which also leads to irregular hysteresis curves.

These issues can cause premature fracture or tearing of gusset plates and middle connections, indicating a limited post-yield capacity and a tendency toward brittle failure modes. As a result, the X-braced frame, while offering increased stiffness, is less suitable for ductile design due to its reduced ductility and energy absorption capacity.

As recognized in seismic design, each structural system exhibits distinct behavioral requirements. For instance, X-braced frames experience significantly higher uplift forces compared to Quasi-X frames, justifying their differing design dimensions. Moreover, as indicated in Table 7, despite the larger column and brace dimensions in the X-braced frame, its hysteretic behavior demonstrates lower energy absorption capacity. This is further corroborated by the premature failure mechanisms and out-of-plane buckling of X-braces, which occur at relatively smaller displacements (Fig. 40).

7. Conclusions

This study investigates both the experimental and numerical aspects of the seismic behavior and failure modes of an innovative multi-story lateral bracing system, the Quasi-X Braced Resisting Frames (QXBRFs), under cyclic quasi-static loading. A comparison was made between QXBRFs and another novel system, the multi-story Elliptic Braced Resisting Frames (ELBRFs), through both experimental testing and numerical simulations. The seismic performance of QXBRFs was also contrasted with that of traditional X-braced frames in a base-story configuration. The study evaluated key parameters such as strength, ductility, stiffness, energy dissipation, and overall seismic performance. Both experimental and numerical findings show strong correlations. The key insights are as follows:

1. Both ELBRF and QXBRF are novel lateral bracing systems that enhance structural performance while addressing facade opening issues common in traditional bracing systems.
2. Elliptic braces, as a novel lateral bracing system, not only create no hindrance to the opening space in the building's facade when installed into the middle bay of the frames but also enhance structural performance as a ductile fuse, resulting in improved energy dissipation and a higher response modification factor.
3. Unlike traditional CBFs, the unique geometry of curve braces enables rapid transition of internal tensile forces to compressive forces as seismic loads fluctuate. The braces quickly return to their original position under compression, preventing permanent deformation or out-of-plane buckling. Seismic tests on steel moment frames with curve braces have shown that this lateral load-resisting system offers a stable, symmetrical hysteresis curve, significant energy dissipation, and retains both strength and stiffness even under large relative displacements.
4. Both ELBRF and QXBRF exhibit stable hysteresis loops and efficient energy dissipation under lateral forces, with no pinching, stiffness degradation, or loss of envelope curve resistance up to approximately 5% drift.
5. ELBRF exhibits higher stiffness and strength compared to QXBRF, largely due to its unique elliptical braces. While both systems show excellent ductility, with plastic deformation progressing from the lower stories upward, ELBRF outperforms QXBRF in strength and energy dissipation.
6. In both ELBRF and QXBRF systems, plastic hinges first form at the elliptic braces, followed by energy absorption. Subsequently, plastic hinges develop at the ends of the beams and columns, preventing early structural collapse.
7. ELBRF's yield strength is 46% higher than QXBRF's, with elastic stiffness 43% greater and post-yielding stiffness 36% higher. ELBRF's softening stiffness is 38% of that of QXBRF.
8. ELBRF dissipates 26% more plastic energy than QXBRF, with hysteresis damping coefficients of 17% for ELBRF and 23% for QXBRF.
9. ELBRF and QXBRF have overstrength factors of 2.50 and 1.80, respectively.
10. The ductility factors for ELBRF and QXBRF are 5.75 and 6.8, respectively.
11. Using the ultimate limit state method, the response modification factors are 7.3 for ELBRF and 6.8 for QXBRF.
12. In the final loading cycles, ELBRF shows minimal strength degradation, while QXBRF experiences a more substantial reduction in strength, including weld fractures at the brace-to-column connections.
13. ELBRF shows a 26% higher energy absorption and dissipation compared to QXBRF during cyclic loading.
14. The columns in ELBRF yield at cycle 22, later than those in QXBRF, which yield at cycle 18. While most braces in ELBRF have yielded, QXBRF shows fewer plastic hinges.
15. Unlike X-braced frames, the elliptic and quarter-elliptic elements in QXBRF revert to their original shape under pressure changes, avoiding permanent deformations and out-of-plane buckling.

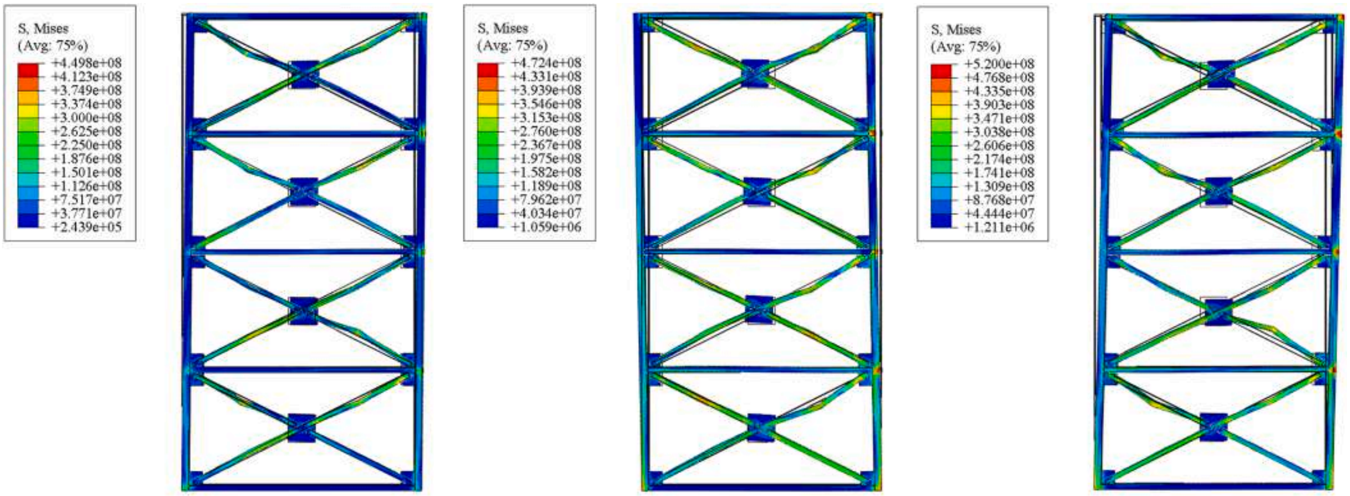

with 20 *mm* displacement, 1.0 % drift

with 40 *mm* displacement, 2.0 % drift

with 60 *mm* displacement, 3.0 % drift

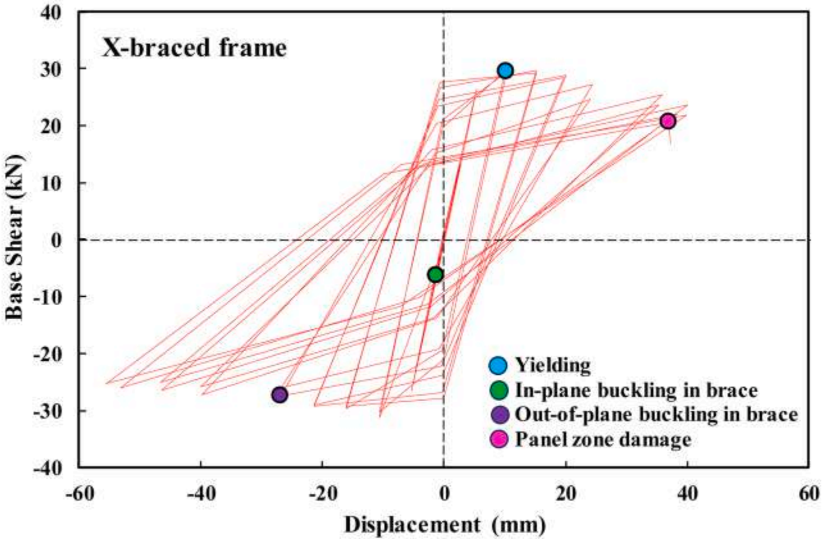

Fig. 40. Deformed shape and Von-Mises stress (Pa) in single-span four-story X-braced frame at different stages of cyclic loading.

16. Numerical simulations using Abaqus software align closely with the experimental data, providing valuable insights into the cyclic behavior of these bracing systems.
17. These results enhance our understanding of these innovative bracing systems, highlighting their potential for use in the design of seismic-resistant steel structures.
18. In ELBRF systems, the force transmission path of the elliptic braces, which are positioned at the center of the columns, does not align perpendicular to the vertical axis, thus preventing column buckling. This gives the system distinct behavior compared to K-braces and diamond braces. The elliptic bracing system demonstrates symmetric behavior under both compression and tension in its hysteresis curve, maintaining strength and stiffness without degradation.
19. The Quasi-X Braced Resisting Frames (QXBRFs) help mitigate the risk of a soft first-story, reduce the asymmetry in behavior between tension and compression, and prevent overall structural instability caused by hardening under large deformations.
20. To further validate and extend the findings of this study, future research should include multi-specimen testing (≥3 identical specimens per configuration) to statistically quantify variability in energy dissipation and failure modes, particularly for critical connections.

CRediT authorship contribution statement

Younes Nouri: Writing – review & editing, Writing – original draft, Visualization, Software, Methodology, Investigation, Data curation, Conceptualization. **Habib Ghasemi Jouneghani:** Writing – review & editing, Writing – original draft, Visualization, Software, Methodology, Investigation, Data curation, Conceptualization. **Abbas Haghollahi:** Writing – review & editing, Validation, Supervision, Formal analysis. **Parham Memarzadeh:** Writing – review & editing, Validation, Supervision, Formal analysis. **Ehsan Hemati:** Software, Methodology, Investigation, Data curation, Conceptualization.

Declaration of competing interest

The authors declare that they have no known competing financial interests or personal relationships that could have appeared to influence the work reported in this paper.

Acknowledgments

This research was supported by the Islamic Azad University of Najafabad (IAUN). The contributions and support from the specialists in the structural laboratory at IAUN are gratefully acknowledged.

Data availability

No data was used for the research described in the article.

References

[1] P. Pan, S. Wu, H. Wang, X. Nie, Seismic performance evaluation of an infilled rocking wall frame structure through quasi-static cyclic testing, Earthq. Eng. Eng. Vib. 17 (2018) 371–383, https://doi.org/10.1007/s11803-018-0447-8.

[2] V. Jaberi, A. Asghari, Seismic behavior of linked column system as a steel lateral force resisting system, J. Constr. Steel Res. 196 (2022) 107428, https://doi.org/10.1016/j.jcsr.2022.107428.

[3] V. Jaberi, Collapse-based design method for simple seismic design of complex structural systems such as linked column frame system, Structures 55 (2023) 482–497, https://doi.org/10.1016/j.istruc.2023.06.059.

[4] V. Jaberi, Collapse-based seismic design method, Adv. Struct. Eng. 28 (2025) 895–918, https://doi.org/10.1177/13694332241291249.

[5] V. Jaberi, A. Asghari, M. Jaberi, Toward collapse-based seismic design of structures: application and implementation in eccentrically braced frames, Iran. J. Sci. Technol. Trans. Civ. Eng. (2025), https://doi.org/10.1007/s40996-025-01741-5.

[6] X. Tong, J.F. Hajjar, A.E. Schultz, C.K. Shield, Cyclic behavior of steel frame structures with composite reinforced concrete infill walls and partially-restrained connections, J. Constr. Steel Res. 61 (2005) 531–552, https://doi.org/10.1016/j.jcsr.2004.10.002.

[7] X. Zhou, Y. He, L. Xu, Q. Zhou, Experimental study and numerical analyses on seismic behaviors of staggered-truss system under low cyclic loading, Thin-Walled Struct. 47 (2009) 1343–1353, https://doi.org/10.1016/j.tws.2009.03.007.

[8] J. Liu, Z. Chen, Y. Liu, Y. Bai, X. Zhong, Full-scale corner-supported modular steel structures with vertical inter-module connections under cyclic loading, J. Build. Eng. 44 (2021) 103269, https://doi.org/10.1016/j.jobe.2021.103269.

[9] L. Fiorino, S. Shakeel, V. Macillo, R. Landolfo, Behaviour factor evaluation the CFS braced structures according to FEMA P695, J. Constr. Steel Res. 138 (2017) 324–339, https://doi.org/10.1016/j.jcsr.2017.07.014.

[10] V. Jaberi, M. Jaberi, A. Asghari, A new performance-based seismic design method using endurance time analysis for linked column frame system and a comparison of structural systems and seismic analysis methods, The Structural Design of Tall and Special Buildings 33 (2024), https://doi.org/10.1002/tal.2100.

[11] A. Asghari, S. Saharkhizan, Seismic design and performance evaluation of steel frames with knee-element connections, J. Constr. Steel Res. 154 (2019) 161–176, https://doi.org/10.1016/j.jcsr.2018.11.011.

[12] S. Sadeghi, F.R. Rofooei, Quantification of the seismic performance factors for steel diagrid structures, J. Constr. Steel Res. 146 (2018) 155–168, https://doi.org/10.1016/j.jcsr.2018.03.018.

[13] Y. Nouri, H.G. Jouneghani, A. Haghollahi, E. Hemati, S.A. Hemati, M. Mortazavi, Experimental and numerical investigation of a steel yielding arc and ring damper, Structures 68 (2024) 107140, https://doi.org/10.1016/j.istruc.2024.107140.

[14] Y. Nouri, H. Ghasemi Jouneghani, A. Shirkhani, E. Hemati, S.A. Hemati, I. Hajirasouliha, Seismic retrofit of steel moment frames with arc and ring yielding dampers: a probabilistic loss assessment using FEMA P-58, Structures 76 (2025) 108898, https://doi.org/10.1016/j.istruc.2025.108898.

[15] M. Farajian, K. Kildashti, P. Sharafi, H. Eslamnia, Quantification of seismic performance factors for modular corner-supported steel bracing system, Structures 45 (2022) 257–274, https://doi.org/10.1016/j.istruc.2022.09.032.

[16] A. Shahiditabar, H. Moharrami, H.H. Snijder, Quantification of seismic performance factors of self-centered y-shaped braced frames, J. Constr. Steel Res. 194 (2022) 107304, https://doi.org/10.1016/j.jcsr.2022.107304.

[17] A. Ashrafi, A. Imanpour, Seismic response of steel multi-tiered eccentrically braced frames, J. Constr. Steel Res. 181 (2021) 106600, https://doi.org/10.1016/j.jcsr.2021.106600.

[18] L. Zheng, S. Dou, S. Tang, H. Ge, W. Wen, J. Zhang, et al., Seismic performance of improved multistorey X-braced steel frames, J. Constr. Steel Res. 212 (2024) 108306, https://doi.org/10.1016/j.jcsr.2023.108306.

[19] H. Ghasemi Jouneghani, A. Haghollahi, H. Moghaddam, Sarvghad Moghadam A. Study of the seismic performance of steel frames in the elliptic bracing, J. Vibroeng. 18 (2016) 2974–2985, https://doi.org/10.21595/jve.2016.16858.

[20] H. Ghasemi Jouneghani, A. Haghollahi, H. Moghaddam, A. Sarveghad Moghadam, Assessing seismic performance of the elliptic braced moment resisting frame through pushover method, J. Rehabil. Civ. Eng. 7 (2019) 68–85, https://doi.org/10.22075/JRCE.2018.13030.1232.

[21] H. Ghasemi Jouneghani, A. Haghollahi, M. Mortazavi, Pushover analysis for estimating seismic demand of elliptic braced moment resisting frames, J. Croat. Assoc. Civ. Eng. 74 (2022) 941–955, https://doi.org/10.14256/JCE.2311.2017.

[22] H. Ghasemi Jouneghani, A.M.M. Haghollahi, Analiza postupnog guranja za procjenu seizmičkih zahtjeva okvira s eliptičnim vezovima, Croat. Assoc. Civ. Eng. 74 (2022) 941–955, https://doi.org/10.14256/JCE.2311.2017.

[23] H. Ghasemi Jouneghani, HA. Experimental study on hysteretic behavior of steel moment frame equipped with elliptical brace, Steel Compos. Struct. 34 (2020) 891–907, https://doi.org/10.12989/scs.2020.34.6.891.

[24] H. Ghasemi Jouneghani, A. Haghollahi, Experimental and analytical study in determining the seismic performance of the ELBRF-E and ELBRF-B braced frames, Steel Compos. Struct. 37 (2020) 571–587, https://doi.org/10.12989/scs.2020.37.5.571.

[25] H. Ghasemi Jouneghani, A. Haghollahi, M. Talebi Kalaleh, B. Beheshti-Aval, Nonlinear seismic behavior of elliptic-braced moment resisting frame using equivalent braced frame, J. Steel Compos. Struct. 40 (2021), https://doi.org/10.12989/scs.2021.40.1.045.

[26] H. Ghasemi Jouneghani, A. Haghollahi, Assessing the seismic behavior of steel moment frames equipped by elliptical brace through incremental dynamic analysis (IDA), Earthq. Eng. Eng. Vib. 19 (2020) 435–449, https://doi.org/10.1007/s11803-020-0572-z.

[27] H. Ghasemi Jouneghani, A. Haghollahi, S.B. Beheshti-Aval, Experimental study of failure mechanisms in elliptic-braced steel frame, Steel Compos. Struct. 37 (2020) 175–191, https://doi.org/10.12989/scs.2020.37.2.175.

[28] H. Ghasemi Jouneghani, N. Fanaie, A. Haghollahi, Theoretical formulation for calculating elastic lateral stiffness in a simple steel frame equipped with elliptic brace, Steel Compos. Struct. 45 (2022) 445–462, https://doi.org/10.12989/scs.2022.45.3.445.

[29] H. Ghasemi Jouneghani, N. Fanaie, M.T. Kalaleh, M. Mortazavi, Determining elastic lateral stiffness of steel moment frame equipped with elliptic brace, Steel Compos. Struct. 46 (2023) 293, https://doi.org/10.12989/scs.2023.46.3.293.

[30] H. Ghasemi Jouneghani, Y. Nouri, M. Mortazavi, A. Haghollahi, P. Memarzadeh, Seismic performance factors of elliptic-braced frames with rotational friction dampers through IDA, Pract. Period. Struct. Des. Constr. 29 (2024) 1–24, https://doi.org/10.1061/PPSCFX.SCENG-1540.

[31] H. Ghasemi Jouneghani, Y. Nouri, P. Memarzadeh, A. Haghollahi, E. Hemati, Seismic performance and failure mechanisms evaluation of multi-story elliptic and mega-elliptic bracing frames: experimental and numerical investigation, Structures 70 (2024) 107658, https://doi.org/10.1016/j.istruc.2024.107658.

[32] A. Shirpour, N. Fanaie, M. Barzegar Seraji, Seismic performance factors of quarter-elliptic-braced steel moment frames (QEB-MFs) using FEMA P695 methodology, Soil Dyn. Earthq. Eng. 178 (2024) 108453, https://doi.org/10.1016/j.soildyn.2024.108453.

[33] A. Shirpour, N. Fanaie, Quantifying the seismic performance factors of half-elliptic-braced steel moment frames (HEB-MFs), Eng. Struct. 311 (2024) 118189, https://doi.org/10.1016/j.engstruct.2024.118189.

[34] N. Fanaie, A. Shirpour, Quasi-X-braced steel moment frames (QXB-MFs) evaluation using analytical and numerical methods, Bull. Earthq. Eng. 22 (2024) 547–582, https://doi.org/10.1007/s10518-023-01778-9.

[35] A. Shirpour, N. Fanaie, Determining the seismic performance factors of Quasi-X bracing systems, J. Constr. Steel Res. 212 (2024) 108248, https://doi.org/10.1016/j.jcsr.2023.108248.

[36] ASTM A370: standard test methods and definitions for mechanical testing of steel products. Mater. Am. Soc. Test., ASTM West Conshohocken; 2014.

[37] American Institute of Steel Construction, ANSI/AISC 360-16: Specification for Structural Steel Buildings, AISC, Chicago, 2016.

[38] K. Hibbitt, Sorensen, ABAQUS/Standard: User's Manual, 1, Hibbitt, Karlsson & Sorensen, 1997.

[39] F. Clauß, M.A. Ahrens, P. Mark, A comparative evaluation of strain measurement techniques in reinforced concrete structures–a discussion of assembly, application, and accuracy, Struct. Concr. 22 (2021) 2992–3007, https://doi.org/10.1002/suco.202000706.

[40] Guidelines for cyclic seismic testing of components of steel structures. (ATC, Appl. Technol. Counc. (1992).

[41] FEMA 356 FE, Prestandard and Commentary for the Seismic Rehabilitation of Buildings, Federal Emergency Management Agency, Washington, DC, USA, 2000.

[42] C.M. Uang, Establishing R (or R and C d factors for building seismic provisions, J. Struct. Eng. 117 (1991) 19–28.

[43] Newmark NM HW, Earthquake Spectra and Design, Earthquake Engineering Research Institute, 1982. El Cerrito, Calif.

[44] T. Liu, B. Briseghella, Q. Zhang, T. Zordan, Equivalent damping of bilinear hysteretic SDOF system considering the influence of initial elastic damping, Soil Dyn. Earthq. Eng. 97 (2017) 74–85, https://doi.org/10.1016/j.soildyn.2017.01.017.

[45] S.M. Zahrai, Cyclic testing of chevron braced steel frames with IPE shear panels, Steel Compos. Struct. 19 (2015) 1167–1184, https://doi.org/10.12989/scs.2015.19.5.1167.

[46] A.A. Chiniforush, A. Ataei, M.A. Bradford, Experimental study of deconstructable bolt shear connectors subjected to cyclic loading, J. Constr. Steel Res. 183 (2021) 106741, https://doi.org/10.1016/j.jcsr.2021.106741.

[47] R. Cornelissen, J. Maljaars, H. Hofmeyer, Buckling and wrinkling of rectangular hollow sections curved in three-point-roll bending, Int. J. Adv. Manuf. Technol. 112 (2021) 2091–2107, https://doi.org/10.1007/s00170-020-06443-y.

[48] X. Zhu, K. Ogi, N. Okabe, Study on wrinkles during rotary-draw bending forming, Mater. Sci. Forum 943 (2019) 43–47, https://doi.org/10.4028/www.scientific.net/MSF.943.43.

[49] J.G. Shin, J.H. Lee, K.Y. Il, H. Yim, Mechanics-based determination of the center roller displacement in three-roll bending for smoothly curved rectangular plates, KSME Int. J. 15 (2001) 1655–1663, https://doi.org/10.1007/BF03185120.

[50] X. Huanga, J. Zhao, A cumulative damage model for extremely low cycle fatigue cracking in steel structure, Struct. Eng. Mech. 62 (2017) 225–236, https://doi.org/10.12989/sem.2017.62.2.225.

[51] X. Huang, C. Wei, J. Zhou, J. Zhao, J. Ge, Experimental and numerical study on ultra low cycle fatigue fracture of X steel tubular joints with CHS braces to SHS chord, Thin-Walled Struct. 162 (2021) 107564, https://doi.org/10.1016/j.tws.2021.107564.

[52] O.W. Blodgett, Design of Welded Structures, Clevel James F. Lincoln Arc Welding Foundation, 1966.

[53] J.H. Thomas, K. Tousignant, Design of single-sided fillet welds under transverse load, J. Struct. Eng. 148 (2022), https://doi.org/10.1061/(ASCE)ST.1943-541X.0003415.

[54] S. Shayan, K.J.R. Rasmussen, H. Zhang, On the modelling of initial geometric imperfections of steel frames in advanced analysis, J. Constr. Steel Res. 98 (2014) 167–177, https://doi.org/10.1016/j.jcsr.2014.02.016.

[55] M.S. Hassan, S. Salawdeh, J. Goggins, Determination of geometrical imperfection models in finite element analysis of structural steel hollow sections under cyclic axial loading, J. Constr. Steel Res. 141 (2018) 189–203, https://doi.org/10.1016/j.jcsr.2017.11.012.

[56] C. Dou, Y.L. Pi, Effects of geometric imperfections on flexural buckling resistance of laterally braced columns, J. Struct. Eng. 142 (2016), https://doi.org/10.1061/(ASCE)ST.1943-541X.0001508.

[57] K. Deng, P. Pan, Y. Su, Y. Xue, Shape optimization of U-shaped damper for improving its bi-directional performance under cyclic loading, Eng. Struct. 93 (2015) 27–35, https://doi.org/10.1016/j.engstruct.2015.03.006.